

Prediction and observation of the first antiferromagnetic topological insulator

M. M. Otrokov,^{1, 2, 3, 4} I. I. Klimovskikh,⁴ H. Bentmann,⁵ D. Estyunin,⁴ A. Zeugner,⁶ Z. S. Aliev,^{7, 8} S. Gaß,⁹ A. U. B. Wolter,⁹ A. V. Koroleva,⁴ A. M. Shikin,⁴ M. Blanco-Rey,^{10, 3} M. Hoffmann,¹¹ I. P. Rusinov,^{12, 4} A. Yu. Vyazovskaya,^{12, 4} S. V. Eremeev,^{13, 12} Yu. M. Koroteev,^{13, 12} V. M. Kuznetsov,¹² F. Freyse,¹⁴ J. Sánchez-Barriga,¹⁴ I. R. Amiraslanov,⁷ M. B. Babanly,¹⁵ N. T. Mamedov,⁷ N. A. Abdullayev,⁷ V. N. Zverev,¹⁶ A. Alfonsov,⁹ V. Kataev,⁹ B. Büchner,^{9, 17} E. F. Schwier,¹⁸ S. Kumar,¹⁸ A. Kimura,¹⁹ L. Petaccia,²⁰ G. Di Santo,²⁰ R. C. Vidal,⁵ S. Schatz,⁵ K. Kißner,⁵ M. Ünzelmann,⁵ C. H. Min,⁵ Simon K. Moser,²¹ T. R. F. Peixoto,⁵ F. Reinert,⁵ A. Ernst,^{11, 22} P. M. Echenique,^{3, 10, 1} A. Isaeva,^{9, 17} and E. V. Chulkov^{10, 3, 1, 4}

¹Centro de Física de Materiales (CFM-MPC), Centro Mixto CSIC-UPV/EHU, 20018 Donostia-San Sebastián, Basque Country, Spain

²IKERBASQUE, Basque Foundation for Science, 48011 Bilbao, Spain

³Donostia International Physics Center (DIPC), 20018 Donostia-San Sebastián, Basque Country, Spain

⁴Saint Petersburg State University, 198504 Saint Petersburg, Russia

⁵Experimentelle Physik VII, Universität Würzburg, Am Hubland, D-97074 Würzburg, Germany

⁶Technische Universität Dresden, Faculty of Chemistry and Food Chemistry, Bergstrasse 66, Dresden, D-01069, Germany

⁷Institute of Physics, Azerbaijan National Academy of Sciences, 1143 Baku, Azerbaijan

⁸Azerbaijan State Oil and Industry University, AZ1010 Baku, Azerbaijan

⁹Leibniz IFW Dresden, Institute for Solid State Research, Helmholtzstrasse 20, D-01069, Germany

¹⁰Departamento de Física de Materiales UPV/EHU, 20080 Donostia-San Sebastián, Basque Country, Spain

¹¹Institut für Theoretische Physik, Johannes Kepler Universität, A 4040 Linz, Austria

¹²Tomsk State University, 634050 Tomsk, Russia

¹³Institute of Strength Physics and Materials Science, Russian Academy of Sciences, 634021 Tomsk, Russia

¹⁴Helmholtz-Zentrum Berlin für Materialien und Energie, Elektronenspeicherring BESSY II, Albert-Einstein-Straße 15, 12489 Berlin, Germany

¹⁵Institute of Catalysis and Inorganic Chemistry, Azerbaijan National Academy of Science, AZ1143 Baku, Azerbaijan

¹⁶Institute of Solid State Physics, Russian Academy of Sciences, Chernogolovka
142432, Russia

¹⁷Technische Universität Dresden, Faculty of Physics, Haeckelstrasse 3, D-01069,
Germany

¹⁸Hiroshima Synchrotron Radiation Center, Hiroshima University, Higashi-Hiroshima,
Hiroshima 739-0046, Japan

¹⁹Department of Physical Sciences, Graduate School of Science, Hiroshima University,
Higashi-Hiroshima, Hiroshima 739-8526, Japan

²⁰Elettra Sincrotrone Trieste, Strada Statale 14 km 163.5, 34149 Trieste, Italy

²¹Advanced Light Source, Lawrence Berkeley National Laboratory, Berkeley, CA
94720, USA

²²Max-Planck-Institut für Mikrostrukturphysik, Weinberg 2, D-06120 Halle, Germany

Corresponding authors: mikhail.otrokov@gmail.com,
evguenivladimirovich.tchoulkov@ehu.eu

(Dated: August 20, 2019)

Magnetic topological insulators (MTIs) are narrow gap semiconductor materials that combine non-trivial band topology and magnetic order¹. Unlike their nonmagnetic counterparts, MTIs may have some of the surfaces gapped due to breaking the time-reversal symmetry, which enables a number of exotic phenomena having potential applications in spintronics¹⁻³. So far, MTIs have only been created by means of doping nonmagnetic TIs with 3d transition metal elements, however, such an approach leads to strongly inhomogeneous magnetic⁴ and electronic⁵ properties of these materials, restricting the observation of important effects to very low temperatures^{2,3}. Finding intrinsic MTI, i.e. a stoichiometric well-ordered magnetic compound, could be an ideal solution to these problems, but no such material was observed to date. Here, using density functional theory we predict and further confirm by means of structural, transport, magnetic, angle- and spin-resolved photoemission spectroscopy measurements the realization of the antiferromagnetic (AFM) TI phase, that is hosted by the van der Waals layered compound MnBi₂Te₄. An interlayer AFM ordering makes MnBi₂Te₄ invariant with respect to the combination of the time-reversal (Θ) and primitive-lattice translation ($T_{1/2}$) symmetries, $S = \Theta T_{1/2}$, giving rise to the Z_2 topological classification of AFM insulators⁶. We find $Z_2 = 1$ for MnBi₂Te₄, which confirms its topologically nontrivial nature. The S -breaking (0001) surface of MnBi₂Te₄ exhibits a giant bandgap in the topological surface state as evidenced by *ab initio* calculations and photoemission measurements. These results culminate almost a decade-long search of an AFMTI,

predicted in 2010⁶. Furthermore, MnBi₂Te₄ is the first intrinsic magnetic TI realized experimentally. As an outcome of this, a number of fundamental phenomena are expected to eventually be observed, being among them quantized magnetoelectric coupling⁶⁻⁸ and axion electrodynamics^{9,10}. Other exotic phenomena could become accessible at temperatures significantly higher than those achieved to date, like the quantum anomalous Hall effect² and chiral Majorana fermions³.

The first reference to MnBi₂Te₄ as a stable chemical compound dates back to 2013 when it was synthesized in the powder form¹¹. The trigonal structure (space group $R\bar{3}m$) of MnBi₂Te₄ comprises of septuple layer (SL) blocks stacked along the [0001] direction and bound to each other by van der Waals forces (Fig. 1a). High-quality MnBi₂Te₄ single crystals were for the first time grown at the TU Dresden (hereinafter D samples, Fig. 2a) and at IP Baku (B samples, Fig. 2b). Our single-crystal X-ray diffraction experiments confirm exactly the same lattice symmetry as reported in Ref. [11]. Since the magnetism of MnBi₂Te₄ was not experimentally investigated, we begin our study by calculating the exchange coupling parameters J from first principles (Figs. 1b and 1c). Among the intralayer interactions J^{\parallel} the one between the first nearest neighbors in the Mn layer is clearly dominant ($J_{0,1}^{\parallel} \approx 0.09 \text{ meV}/\mu_B^2$), while the interactions with more distant neighbors are an order of magnitude weaker, whereupon an FM ordering is expected within each SL block of MnBi₂Te₄. In contrast, the interlayer coupling constants J^{\perp} are mostly negative resulting in a negative $J_0^{\perp} \approx \sum_{j \neq 0} J_{0,j}^{\perp}$ coefficient equal to $-0.022 \text{ meV}/\mu_B^2$, which means that the overall coupling between neighboring Mn layers is antiferromagnetic (Fig. 1d). The magnetic anisotropy energy is positive and equal to 0.225 meV per Mn atom, indicating the easy axis with an out-of-plane orientation of the local magnetic moments (LMMs) of $\pm 4.607\mu_B$. Monte Carlo simulations confirm the interlayer AFM structure with a Néel temperature (T_N) of 3D ordering of 25.4 K (Extended Data Fig. 1).

Given the magnetic ground state, the bulk electronic structure was calculated. As shown in Fig. 1e, the system is insulating, the fundamental bandgap value, determined from the GGA+ U calculation of the density of states (DOS), is of $\sim 220 \text{ meV}$. To determine whether the gap is negative (inverted), we performed the DOS calculations decreasing the spin-orbit coupling (SOC) constant λ stepwise from its natural value λ_0 to $\lambda = 0.5\lambda_0$. It was found that at $\lambda/\lambda_0 \approx 0.675$ the gap is closed, while at other λ/λ_0 ratios it is nonzero, which points towards a nontrivial topology of MnBi₂Te₄.

Mong, Essin, and Moore⁶ introduced a Z_2 classification of AFM insulators, provided by the $S = \Theta T_{1/2}$ -symmetry, which is inherent to MnBi₂Te₄. We find $Z_2 = 1$, which classifies MnBi₂Te₄ as an AFMTI.

The implication of the bulk bandgap inversion in a TI is seen at its surface, where the topological phase manifests itself by the appearance of the topological surface state. In the case of nonmagnetic TIs, this surface state is gapless¹², however at the (0001) surface of the AFMTI MnBi₂Te₄ we find a 88-meV-wide bandgap (Fig. 1f). Here, the S -symmetry is broken and the out-of-plane magnetization of the near-surface FM layer opens the Dirac

point (DP) gap⁶. In contrast, the S -preserving surface is gapless as it should be for an AFMTI (inset to Fig. 1f and Extended Data Fig. 2).

Temperature- and field-dependent magnetization measurements performed on D samples (Fig. 2c,d) establish a 3D AFM order below $T_N = 24.2(5)$ K, in agreement with the prediction by Monte Carlo method and results of the resistivity measurements (Extended Data Fig. 3a). Below T_N , a strongly anisotropic magnetic susceptibility χ is observed, that decreases much steeper for $H \perp (0001)$. No splitting between zero-field-cooled and field-cooled-warming curves was found. The paramagnetic (PM) regime above T_N was fitted with a modified Curie-Weiss law, $\chi(T) = \chi_0 + C/(T - \Theta_{CW})$, in the 100 K to 250 K range. Here, χ_0 stands for a temperature-independent magnetic susceptibility of both diamagnetic closed electron shells and a Pauli PM contribution due to some degree of metallicity in this material (see below). $C/(T - \Theta_{CW})$ considers a temperature-dependent Curie-Weiss susceptibility of the Mn LMMs. The fitted effective PM moment of $5.0(2)\mu_B$ is in rough agreement with the high-spin configuration of Mn^{2+} ($S = 5/2$), while a small and positive value of the Curie-Weiss temperature ($\Theta_{CW} = 3(3)$ K) strongly depends on the fitted χ_0 contribution. The $M(H)$ curve acquired below T_N for $H \perp (0001)$ shows an indicative spin-flop transition at $\mu_0 H_{SF} \approx 3.5$ T (Fig. 2d), which is in line with an out-of-plane easy axis of the staggered magnetization.

We further performed X-ray magnetic circular dichroism (XMCD) experiments at the Mn $L_{2,3}$ absorption edge (Fig. 2e; D samples). The data were acquired in total electron yield (TEY) mode with a probing depth of typically only a few nm. The XMCD signal obtained at an external field of 6 T and in normal light incidence verifies a magnetic polarization of the Mn ions. After removing the external field ($H = 0$) the signal collapses as expected for an AFM ordering. Yet, a small residual signal is observed in remanence, indicating a finite net out-of-plane polarization within the probed volume of the sample. This residual signal appears to be inconsistent with an AFM intralayer coupling where the orientation of the moments within a Mn layer alternates on the atomic scale. For FM intralayer coupling, however, the first SL, which is preferentially probed in the TEY mode, is expected to be composed of mesoscopic domains with the magnetization pointing in or out of the surface plane. We attribute the residual XMCD signal in remanence to a preferential sampling of one domain type with the micron-sized synchrotron beam spot. This supports our first-principles calculations predicting an FM ordering within individual SLs. Performing the same experiment in grazing light incidence, i.e. with sensitivity to in-plane magnetization, we observe no finite polarization in remanence.

Altogether, the experimental scope of evidence (Fig. 2) allows identifying $MnBi_2Te_4$ as an interlayer antiferromagnet, in which FM Mn layers are coupled antiparallel to each other and the easy axis of staggered magnetization points perpendicular to the layers (Fig. 1d).

The surface electronic structure of $MnBi_2Te_4(0001)$ was studied using angle-resolved photoemission spectroscopy (ARPES). The intensity map measured near the Brillouin zone center at a temperature of 17 K is shown in Fig. 3a ($h\nu = 28$ eV; B sample). One can

clearly see two almost linearly dispersing bands forming a Dirac-cone-like structure with strongly reduced intensity at the crossing point. The energy distribution curves (EDCs) reveal an energy gap of about 70 meV at the $\bar{\Gamma}$ -point that separates the upper and lower parts of the cone (Fig. 3b). A similar result was obtained for the D samples (Extended Data Fig. 4). These results agree with those of the $\text{MnBi}_2\text{Te}_4(0001)$ surface bandstructure calculations (see Fig. 1f).

Next, we performed extensive ARPES measurements with different photon energies. At $h\nu = 9$ eV (Fig. 3c), the features different from those seen at $h\nu = 28$ eV show a pronounced spectral weight: namely, the intense electron- and hole-like bands coming to the $\bar{\Gamma}$ -point at binding energies of about 0.17 eV and 0.4 eV, respectively. A comparison with the theoretically calculated bulk-projected bandstructure allows identifying these bands as the bulk conduction and valence bands, respectively. The analysis of the $\bar{\Gamma}$ -point EDC shows that both valence and conduction bands can be fitted with two peaks (Extended Data Fig. 5) in agreement with the result of our calculations, showing two bulk bands with a weak k_z dispersion both below and above the Fermi level (Fig. 1f). Based on the photoemission measurements, we estimate the bulk bandgap to be close to 200 meV, again, in agreement with the calculated values. The second derivative data in the inset to Fig. 3c provide further insight, apart from the bulk bands revealing also the gapped Dirac cone. Note that the Fermi level cuts the conduction band, indicating the n -doped character of the samples, which is consistent with the results of the Hall measurements (see Extended Data Fig. 3b). If we artificially drive MnBi_2Te_4 into a topologically-trivial phase by decreasing the SOC strength in a calculation, a strong discrepancy arises between the theory and experiment. Namely, in the trivial phase there are no surface states in the fundamental bulk bandgap (Extended Data Fig. 6). In contrast, the ARPES data acquired at different photon energies (Extended Data Fig. 7) unambiguously confirm the gapped Dirac cone to be a surface state, in agreement with the calculated (0001) surface bandstructure of the MnBi_2Te_4 AFMTI (Fig. 1f).

Thus, in virtue of the good agreement between the theory and experiment, we conclude that the fundamental bandgap of MnBi_2Te_4 is inverted. Our data also confirm the trigonal structure (sp. gr. $R\bar{3}m$) and interlayer AFM order, whereby the S -symmetry is confirmed, too. All this proves the $Z_2 = 1$ 3D AFMTI phase in MnBi_2Te_4 below its Néel temperature, which thus is the first experimentally identified system in the AFMTI class.

The ARPES measurements above T_N were performed next. Remarkably, increasing the temperature does not lead to the DP gap closing at $\text{MnBi}_2\text{Te}_4(0001)$, see Fig. 3d. Nevertheless, we observe a temperature dependence of a linear dichroism in the Dirac cone intensity that indicates an influence of the AFM order on the topological surface state (see Extended Data Fig. 8). Moreover, straight below T_N , the intensity of the Dirac cone starts to grow abruptly when the temperature decreases (Fig. 3e and Extended Data Fig. 9; laser ARPES with $h\nu = 6.4$ eV), signaling the paramagnet-antiferromagnet transition and showing a clear response of the surface electronic structure to the AFM ordering. In Fig. 3f, the photoemission intensity map acquired at $T = 10.5$ K is shown. A closer look at these data around the DP gap (Fig. 3g) and their comparison to the

analogous spectrum taken at 35 K (Fig. 3h) reveals that significant changes occur across the Néel temperature. In particular, the shape of the $\bar{\Gamma}$ -point EDC is modified: a pronounced intensity dip due to the DP gap at ~ 0.28 eV seen at 10.5 K (Fig. 3g) is absent at 35 K (Fig. 3h). Nevertheless the DP gap is present in Fig. 3h, as the EDC fit was only possible with two peaks, corresponding to the DP gap edges. Thus, while the antiferromagnet-paramagnet transition does not lead to the DP gap closing, the results in Figs. 3e-h reveal clearly the strong sensitivity of the topological surface state to the AFM ordering. The presence of a DP gap in the PM phase was previously reported for the surface states of magnetically-doped TIs¹³⁻¹⁵. In the case of the $\text{Bi}_{2-x}\text{Mn}_x\text{Se}_3(0001)$ surface, resonant scattering processes due to impurity in-gap states were suggested to be a possible reason of such behavior¹⁵. To check whether similar effects take place in our MnBi_2Te_4 samples, we performed resonant photoemission measurements at the Mn $3p-3d$ edge. The results, shown in Fig. 3i, reveal no resonant features and, hence, no Mn- $3d$ -DOS around the DP gap, whereupon we discard such a mechanism of the DP gap opening in MnBi_2Te_4 .

To get a deeper insight into the electronic properties of MnBi_2Te_4 both below and above T_N , we performed electron spin resonance (ESR) measurements (Fig. 4a; D samples). In MnBi_2Te_4 , the ESR linewidth $\Delta H(T)$ shows a quite surprising anisotropic behavior above ~ 50 K. Namely, the so-called Korringa slope $b = d[\Delta H(T)]/dT$ of the linear $\Delta H(T)$ dependence for $H \perp (0001)$ is three times larger than that for $H \parallel (0001)$ (Fig. 4a), suggesting spatially anisotropic fluctuations of the LMMs due to their coupling to conduction electrons^{16,17}. The fact that in MnBi_2Te_4 $b_{\perp} \gg b_{\parallel}$ indicates a relatively short transversal relaxation time τ_2 of the LMMs for the out-of-plane static field geometry and, thus, fast fluctuations of the Mn spins in the (0001) plane. In contrast, in the case of the in-plane field geometry, where the τ_2 relaxation time characterizes Mn spin fluctuations perpendicular to the (0001) plane, the fluctuations appear to be significantly slower, as reflected in the smaller b_{\parallel} . Consequently, on a timescale of the photoexcitation process in ARPES ($\sim 10^{-15}$ seconds), which is much shorter than the Mn spins relaxation time ($\sim 10^{-10}$ seconds), the probability to find the Mn spin oriented perpendicular to (0001) may be larger than for other directions, which could effectively generate an instantaneous out-of-plane field acting on the topological surface state electrons even in the absence of long-range order. Indeed, our room temperature spin-ARPES measurements reveal the out-of-plane spin components both at the $\bar{\Gamma}$ -point (Fig. 4b) and at finite k_{\parallel} (see Extended Data Fig. 10). Moreover, the calculated paramagnons indicate a presence of FM correlations within individual SL blocks above T_N (right inset to Fig. 4a). At that, the FM-correlated moments tend to point perpendicular to the (0001) plane, which is consistent with the spin-ARPES observations, revealing out-of-plane spin polarization near the Fermi level. We thus conclude that the instantaneous out-of-plane spin polarization observed in our experiments could be responsible for the persistence of the DP gap observed by ARPES in the PM state of MnBi_2Te_4 .

Our experimental and theoretical results establish MnBi_2Te_4 as the first observed AFMTI. Although in our experiment MnBi_2Te_4 is n -doped (which is typical for the Bi-based bulk

TI crystals), it is n -doping that allows measuring both the topological surface state and the bulk energy gap with ARPES, which probes only the occupied states. A common strategy in synthesizing truly insulating TI crystals is Sb-doping of the Bi sublattice of tetradymite-like compounds^{2,18}, which is expected to work for MnBi_2Te_4 as well. Note that such a tuning of composition is not supposed to affect its interlayer AFM ordering¹⁹. On the other hand, recent progress in the molecular beam epitaxy growth of the TI films²⁰ rises hope that a nearly charge neutral MnBi_2Te_4 can be fabricated.

All this would constitute an important step towards many novel applications. Indeed, according to Ref. [6], an AFMTI with the type of antiferromagnetic order established here for MnBi_2Te_4 represents ideal platform for observing the half-integer quantum Hall effect ($\sigma_{xy} = e^2/(2h)$), which may facilitate experimental confirmation of the $\theta = \pi$ quantized magnetoelectric coupling. A material showing this effect is known as an axion insulator, which up to now was being sought for in magnetically-doped sandwich-like TI heterostructures^{21,22}. Unfortunately, the latter were found to show superparamagnetic behavior^{4,23} – a drawback that MnBi_2Te_4 does not suffer from, which makes it a promising intrinsic axion insulator candidate. On the other hand, the FM SL blocks of MnBi_2Te_4 can be utilized for the fabrication of topologically-nontrivial heterostructures^{24,25}, which are promising for the quantum anomalous Hall effect². Beyond topotronics, another direction of further studies of MnBi_2Te_4 and related materials^{19,26-29} lies within the rapidly growing field of van der Waals magnets^{30,31}. Strongly thickness-dependent properties, expected for the van der Waals compounds in the 2D limit, combined with the magnetic degrees of freedom and strong SOC of MnBi_2Te_4 , make it an interesting candidate to couple the emerging fields of antiferromagnetic spintronics^{32,33} and layered van der Waals materials^{30,31}.

We have become aware of recent theoretical^{34,35} and experimental³⁶⁻⁴² studies on MnBi_2Te_4 that confirm our results. In particular, the intrinsic axion insulator state has just been realized in the AFM (i.e. below the Néel temperature) MnBi_2Te_4 thin flakes exfoliated from a bulk single crystal⁴¹, providing an additional proof of the AFMTI state in MnBi_2Te_4 below T_N . Besides, the quantized Hall effect under external magnetic field has been achieved in such flakes⁴⁰⁻⁴². Although the observation of this effect requires ferromagnetic state of MnBi_2Te_4 , it would not be observed if MnBi_2Te_4 was topologically trivial⁴³.

1. Tokura, Y., Yasuda, K. & Tsukazaki, A. Magnetic topological insulators. *Nature Reviews Physics* **1**, 126-143 (2019).
2. Chang, C.-Z. et al. Experimental observation of the quantum anomalous Hall effect in a magnetic topological insulator. *Science* **340**, 167-170 (2013).
3. He, Q. L. et al. Chiral Majorana fermion modes in a quantum anomalous Hall insulator-superconductor structure. *Science* **357**, 294-299 (2017).
4. Lachman, E. O. et al. Visualization of superparamagnetic dynamics in magnetic topological insulators. *Sci. Adv.* **1**, e1500740 (2015).

5. Lee, I. et al. Imaging Dirac-mass disorder from magnetic dopant atoms in the ferromagnetic topological insulator $\text{Cr}_x(\text{Bi}_{0.1}\text{Sb}_{0.9})_{2-x}\text{Te}_3$. Proceedings of the National Academy of Sciences **112**, 1316-1321 (2015).
6. Mong, R. S. K., Essin, A. M. & Moore, J. E. Antiferromagnetic topological insulators. Phys. Rev. B **81**, 245209 (2010).
7. Qi, X.-L., Hughes, T. L. & Zhang, S.-C. Topological field theory of time-reversal invariant insulators. Phys. Rev. B **78**, 195424 (2008).
8. Essin, A. M., Moore, J. E. & Vanderbilt, D. Magnetoelectric polarizability and axion electrodynamics in crystalline insulators. Phys. Rev. Lett. **102**, 146805 (2009).
9. Li, R., Wang, J., Qi, X.-L. & Zhang, S.-C. Dynamical axion field in topological magnetic insulators. Nat. Phys. **6**, 284-288 (2010).
10. Wang, J., Lian, B. & Zhang, S.-C. Dynamical axion field in a magnetic topological insulator superlattice. Phys. Rev. B **93**, 045115 (2016).
11. Lee, D. S. et al. Crystal structure, properties and nanostructuring of a new layered chalcogenide semiconductor, Bi_2MnTe_4 . CrystEngComm **15**, 5532-5538 (2013).
12. Hasan, M. Z. & Kane, C. L. Colloquium: Topological insulators. Rev. Mod. Phys. **82**, 3045-3067 (2010).
13. Chen, Y. L. et al. Massive Dirac fermion on the surface of a magnetically doped topological insulator. Science **329**, 659-662 (2010).
14. Xu, S.-Y. et al. Hedgehog spin texture and Berry's phase tuning in a magnetic topological insulator. Nat. Phys. **8**, 616-622 (2012).
15. Sánchez-Barriga, J. et al. Nonmagnetic band gap at the Dirac point of the magnetic topological insulator $(\text{Bi}_{1-x}\text{Mn}_x)_2\text{Se}_3$. Nat. Commun. **7**, 10559 (2016).
16. Vaknin, D., Davidov, D., Zevin, V. & Selig, H. Anisotropy and two-dimensional effects in the ESR properties of OsF_6 -graphite intercalation compounds. Phys. Rev. B **35**, 6423 (1987).
17. Vithayathil, J. P., MacLaughlin, D. E., Koster, E., Williams, D. L. & Bucher, E. Spin fluctuations and anisotropic nuclear relaxation in single-crystal UPT_3 . Phys. Rev. B **44**, 4705 (1991).
18. Zhang, J., Chang, C.-Z., Zhang, Z. & et al. Band structure engineering in $(\text{Bi}_{1-x}\text{Sb}_x)_2\text{Te}_3$ ternary topological insulators. Nat. Commun. **2**, 574 (2011).
19. Eremeev, S. V., Otrokov, M. M. & Chulkov, E. V. Competing rhombohedral and monoclinic crystal structures in MnPn_2Ch_4 compounds: An *ab-initio* study. J. Alloys Compd. **709**, 172-178 (2017).
20. Wu, L. et al. Quantized Faraday and Kerr rotation and axion electrodynamics of a 3D topological insulator. Science **354**, 1124-1127 (2016).
21. Mogi, M. et al. A magnetic heterostructure of topological insulators as a candidate for an axion insulator. Nat. Mater. **16**, 516-521 (2017).
22. Xiao, D. et al. Realization of the axion insulator state in quantum anomalous Hall sandwich heterostructures. Phys. Rev. Lett. **120**, 056801 (2018).
23. Krieger, J. A. et al. Spectroscopic perspective on the interplay between electronic and magnetic properties of magnetically doped topological insulators. Phys. Rev. B **96**, 184402 (2017).

24. Otrokov, M. M. et al. Magnetic extension as an efficient method for realizing the quantum anomalous Hall state in topological insulators. *JETP Lett.* **105**, 297-302 (2017).
25. Otrokov, M. M. et al. Highly-ordered wide bandgap materials for quantized anomalous Hall and magnetoelectric effects. *2D Mater.* **4**, 025082 (2017).
26. Hirahara, T. et al. Large-gap magnetic topological heterostructure formed by subsurface incorporation of a ferromagnetic layer. *Nano Lett.* **17**, 3493-3500 (2017).
27. Hagmann, J. A. et al. Molecular beam epitaxy growth and structure of self-assembled $\text{Bi}_2\text{Se}_3/\text{Bi}_2\text{MnSe}_4$ multilayer heterostructures. *New J. Phys.* **19**, 085002 (2017).
28. Rienks, E. D. L. et al. Large magnetic gap at the Dirac point in a Mn-induced Bi_2Te_3 heterostructure. Preprint arXiv:1810.06238 (2018).
29. Ereemeev, S. V., Otrokov, M. M., & Chulkov, E. V. New universal type of interface in the magnetic insulator/topological insulator heterostructures. *Nano Lett.* **18**, 6521-6529 (2018).
30. Gong, C. et al. Discovery of intrinsic ferromagnetism in two-dimensional van der Waals crystals. *Nature* **546**, 265-269 (2017).
31. Huang, B. et al. Layer-dependent ferromagnetism in a van der Waals crystal down to the monolayer limit. *Nature* **546**, 270-273 (2017).
32. Baltz, V. et al. Antiferromagnetic spintronics. *Rev. Mod. Phys.* **90**, 015005 (2018).
33. Smejkal, L., Mokrousov, Y., Yan, B. & MacDonald, A. H. Topological antiferromagnetic spintronics. *Nat. Phys.* **14**, 242-251 (2018).
34. Zhang, D. et al. Topological axion states in magnetic insulator MnBi_2Te_4 with the quantized magnetoelectric effect. Preprint arXiv:1808.08014 (2018).
35. Li, J. et al. Intrinsic magnetic topological insulators in van der Waals layered MnBi_2Te_4 -family materials. Preprint arXiv:1808.08608 (2018).
36. Gong, Y. et al. Experimental realization of an intrinsic magnetic topological insulator. Preprint arXiv:1809.07926 (2018).
37. Lee, S. H. et al. Spin scattering and noncollinear spin structure-induced intrinsic anomalous Hall effect in antiferromagnetic topological insulator MnBi_2Te_4 . Preprint arXiv:1812.00339 (2018).
38. Yan, J.-Q. et al. Crystal growth and magnetic structure of MnBi_2Te_4 . Preprint arXiv:1902.10110 (2019).
39. Chen, B. et al. Searching the $\text{Mn}(\text{Sb},\text{Bi})_2\text{Te}_4$ family of materials for the ideal intrinsic magnetic topological insulator. Preprint arXiv:1903.09934 (2019).
40. Deng, Y. et al. Magnetic-field-induced quantized anomalous Hall effect in intrinsic magnetic topological insulator MnBi_2Te_4 . Preprint arXiv:1904.11468 (2019).
41. Liu, C. et al. Quantum phase transition from axion insulator to Chern insulator in MnBi_2Te_4 . Preprint arXiv:1905.00715 (2019).
42. Ge, J. et al. High-Chern-Number and High-Temperature Quantum Hall Effect without Landau Levels. Preprint arXiv:1907.09947 (2019).

43. Otrokov, M.M. et al. Unique thickness-dependent properties of the van der Waals interlayer antiferromagnet MnBi_2Te_4 films. *Phys. Rev. Lett.* **122**, 107202 (2019).

Acknowledgments

M.M.O. and E.V.C. thank A. Arnau and J. I. Cerdá for stimulating discussions. We acknowledge the support by the Basque Departamento de Educacion, UPV/EHU (Grant No. IT-756-13), Spanish Ministerio de Economia y Competitividad (MINECO Grant No. FIS2016-75862-P), and Academic D.I. Mendeleev Fund Program of Tomsk State University (Project No. 8.1.01.2018). The supports by the Saint Petersburg State University grant for scientific investigations (Grant No. 15.61.202.2015), Russian Science Foundation (Grant No. 18-12-00062), Russian Foundation for Basic Research (Grant No. 18-52-06009), and the Science Development Foundation under the President of the Republic of Azerbaijan (Grant No. EIF-BGM-4-RFTF-1/2017-21/04/1-M-02) are also acknowledged. M.M.O. acknowledges support by the Diputación Foral de Gipuzkoa (project no. 2018-CIEN-000025-01). I.I.K. and A.M.S. acknowledge partial support from the CERIC-ERIC consortium for the stay at the Elettra synchrotron. The support by the German Research Foundation (DFG) is acknowledged by A.U.B.W., A.I., and B.B. within the Collaborative Research Center 1143, by A.Z., A.E., and A.I. within of the Special Priority Program 1666 Topological Insulators, by H.B. and F.R. within the Collaborative Research Center 1170, and by A.Z. and A.I. within the ERANET-Chemistry Program (RU 776/15-1). H.B., A.U.B.W., A.A., V.K., B.B., F.R. and A.I. acknowledge financial support from the DFG through Würzburg-Dresden Cluster of Excellence on Complexity and Topology in Quantum Matter - ct.qmat (EXC 2147, project-id 39085490). A.E. acknowledges support by the OeAD grants No. HR 07/2018 and PL 03/2018. This work was also supported by the Fundamental Research Program of the State Academies of Sciences, line of research III.23. A.K. was financially supported by KAKENHI number 17H06138 and 18H03683. I.P.R. acknowledges support by the Ministry of Education and Science of the Russian Federation within the framework of the governmental program Megagrants (state task no. 3.8895.2017/P220). The calculations were performed in Donostia International Physics Center, in the Research park of St. Petersburg State University Computing Center (<http://cc.spbu.ru>), and in Tomsk State University.

Author Contributions

The bandstructure calculations were performed by M.M.O., M.B.R., S.V.E, and A.Yu.V. The exchange coupling constants calculations were performed by M.B.R., Yu.M.K., M.M.O., and A.E. The paramagnons calculations were performed by A.E. The magnetic anisotropy studies were performed by M.M.O. The Monte Carlo simulations were performed by M.H. The topological invariant calculations were done by S.V.E. Tight-binding calculations were performed by I.P.R. and V.M.K. Crystals were grown by A.Z., A.I., Z.S.A., and M.B.B. X-ray diffraction measurements and structure determination were performed by A.Z., and I.R.A. The resistivity and Hall measurements, as well as contact preparation were done by N.T.M., N.A.A., and V.N.Z. XMCD and resonant

photoemission experiments were performed by R.C.V., T.R.F.P., C.H.M., S.M., K.K., S.S., and H.B. Magnetization experiments and their analysis were mainly performed by S.G., B.B., and A.U.B.W. with contributions by A.V.K. ARPES measurements were done by I.I.K., D.E., A.M.S., E.F.S., S.K., A.K., L.P., G.D.S., H.B., and M.Ü. The analysis of the ARPES data was done by I.I.K., D.E., H.B., and M.Ü. Spin-ARPES measurements were performed by I.I.K., D.E., A.M.S., F.F., and J.S.-B. ESR measurements were done by A.A. and V.K. The project was planned by M.M.O., A.I., H.B., A.M.S., N.T.M., F.R., P.M.E., and E.V.C. The supervision of the project was executed by E.V.C. All authors contributed to the discussion and manuscript editing. The paper was written by M.M.O. with contributions by A.I., H.B., V.K. and A.U.B.W.

Reprints and permissions

Reprints and permissions information is available at www.nature.com/reprints.

Competing financial interest

Authors declare no competing financial interests.

Correspondence and requests

Correspondence and requests for materials should be addressed to mikhail.otrokov@gmail.com.

Main figure legends

Figure 1. Theoretical insight into the crystal, magnetic and electronic structure of MnBi_2Te_4 . **a**, Crystal structure of the trigonal MnBi_2Te_4 with yellow, blue and green balls showing Mn, Te and Bi atoms, respectively. The “nonmagnetic” rhombohedral primitive unit cell is shown by grey lines, the $T_{1/2}$ translation is shown in magenta; “vdW” stands for van der Waals. **b**, Calculated exchange constants $J_{0,j}$ (in meV/μ_B^2) for the intralayer (J^{\parallel} , red circles) and interlayer (J^{\perp} , blue squares) pair interactions as a function of the Mn-Mn distance, $r_{0,j}$ (in Å). **c**, Schematic top view representation of magnetic interactions in the Mn layer (upper part) and between two neighboring Mn layers (lower part). **d**, Magnetic unit cell corresponding to the interlayer AFM state. **e**, Total DOS of bulk MnBi_2Te_4 calculated for the interlayer AFM state shown in **d** using the HSE06 exchange-correlation functional (dash-point black line) and the GGA+ U approach (solid color lines). In the latter case, the evolution of the DOS with the change of the SOC constant λ is shown. **f**, Spin-resolved electronic structure of the $\text{MnBi}_2\text{Te}_4(0001)$ surface. The size of color circles reflects the value and sign of the spin vector Cartesian projections, with red/blue colors corresponding to the positive/negative s_x and s_y components (perpendicular to k_{\parallel}), and gold/cyan to the out-of-plane components $+s_z/-s_z$. The green areas correspond to the bulk bandstructure projected onto the surface Brillouin zone. The left-hand inset of panel **f** shows the tight-binding calculated electronic bandstructure of the S -preserving $(10\bar{1}1)$ surface (see also Extended Data Fig. 2). The regions with a

continuous spectrum correspond to the 3D bulk states projected onto the 2D Brillouin zone.

Figure 2. MnBi₂Te₄ single crystals and their magnetic properties. **a, b**, MnBi₂Te₄ single crystals: D sample (**a**, optical microscope image) and B sample (**b**, scanning electron microscope image). **c**, Magnetic susceptibility (left axis of ordinates) of phase-pure MnBi₂Te₄ as a function of temperature measured in an external magnetic field of $\mu_0 H = 1$ T in zero-field-cooled (zfc) and field-cooled-warming (fcw) conditions along with the temperature-dependent reciprocal susceptibility (right axis of ordinates) for $H \perp (0001)$. The green line is a modified Curie-Weiss fit to the high-temperature data ($\chi_0 = 0.0028(3)$ emu/mol Oe); for details see text. **d**, Field-dependent magnetization curves for the two directions measured at 2 and 300 K. **e**, X-ray magnetic circular dichroism measurements for MnBi₂Te₄ at the Mn $L_{2,3}$ edge. A sketch of the experiment is given in the inset. The external magnetic field is applied along the direction of light incidence. The two top panels show the sum (XAS signal) and the difference (XMCD signal) between the I_R and I_L X-ray absorption intensities measured with right and left circularly polarized light in normal incidence at $\mu_0 H = 6$ T. The bottom panels show the XMCD signal in remanence, i.e. at $H = 0$ T, for normal and grazing light incidence, measured after switching off an external field of $\mu_0 H = 6$ T along the respective directions. Insets show a magnification of the L_3 dichroism in remanence.

Figure 3. Photoemission spectroscopy insight into the surface and bulk bandstructure of MnBi₂Te₄. **a**, Dispersion of MnBi₂Te₄(0001) measured at 17 K with a photon energy of 28 eV and **b**, EDC representation of the data shown in **a**. The red curve marks the EDC at the $\bar{\Gamma}$ -point. **c**, Dispersion of MnBi₂Te₄(0001) measured at the same temperature with a photon energy of 9 eV (which is more bulk sensitive) with the corresponding second derivative, $d^2N(E)/dE^2$, shown in the inset; BVB and BCB stand for the bulk valence and conduction bands, respectively. **d**, ARPES image acquired at 300 K ($h\nu = 28$ eV). **e**, Temperature dependence of the Dirac surface state photoemission intensity calculated as a sum of the intensities of the lower and upper parts of the cone at the $\bar{\Gamma}$ -point (see Methods section for further details). **f**, The same as **c**, but measured with laser photon energy of 6.4 eV, $T = 10.5$ K, and a different sample. A small dashed rectangle around the DP marks the region that is further magnified in **g**. **g, h** Zooms into the DP gap region of the ARPES maps taken at 10.5 and 35 K, respectively, with the fitted EDC spectra at the $\bar{\Gamma}$ -point plotted on top. The raw data, resulting fitted curves, and their decompositions with Voigt peaks are shown by blue circles, black/white lines, and grey/red lines, respectively. Red (grey) lines indicate the peaks attributed to the gapped Dirac cone state (bulk bands). The results shown in **a-h** were acquired on B samples. **i**, Resonant valence band spectra of MnBi₂Te₄ taken at the Mn $3p-3d$ absorption edge (D samples). On- and off-resonance spectra were obtained at $h\nu = 51$ eV and $h\nu = 47$ eV, respectively. The difference between these spectra approximately reflects the Mn $3d$ DOS showing a main peak near 3.8 eV and an additional feature near 1 eV. The energy range of the bulk energy gap is marked by a cyan stripe.

Figure 4. Spin characterization of bulk and surface electronic structure of MnBi_2Te_4 . **a**, Typical ESR spectra (field derivative of the microwave absorption $dP(H)/dH$) of Mn^{2+} in MnBi_2Te_4 at $\nu = 9.6$ GHz (left inset) and T -dependence of the width ΔH of the ESR signal (main panel) for two directions of the magnetic field. Dashed lines are linear fits to the $\Delta H(T)$ dependence yielding the Korringa slopes $b_{\perp,\parallel} = d[\Delta H(T)/dT]$. The error bars are defined from the fitting procedure of ESR line shapes. The larger error bars above ~ 100 K are due to the occurrence of a parasitic signal in the ESR spectrum overlapping with the main line. The measurements were done on D samples. See Methods section for more information about ESR measurements of MnBi_2Te_4 . The right inset of panel **a** shows a magnon spectrum calculated *ab initio* for bulk MnBi_2Te_4 in the PM state (paramagnons). **b**, Room temperature spin-resolved ARPES spectra measured at the $\bar{\Gamma}$ -point with respect to the out-of-plane spin quantization axis. The out-of-plane spin polarization is presented below the corresponding spin-up and spin-down spectra. The inset shows the spin-integrated ARPES spectrum taken along the $\bar{K} - \bar{\Gamma} - \bar{K}$ direction. Yellow and cyan curves show the location of the gapped Dirac cone. The data were obtained for B sample at photon energy of 6 eV. See Extended Data Fig. 10 for more spin-resolved ARPES data.

METHODS

Electronic structure and total-energy calculations

Electronic structure calculations were carried out within the density functional theory using the projector augmented-wave (PAW) method⁴⁴ as implemented in the VASP code^{45,46}. The exchange-correlation energy was treated using the generalized gradient approximation⁴⁷. The Hamiltonian contained scalar relativistic corrections and the SOC was taken into account by the second variation method⁴⁸. In order to describe the van der Waals interactions we made use of the DFT-D2⁴⁹ and the DFT-D3^{50,51} approaches, which gave similar results. The energy cutoff for the plane-wave expansion was set to 270 eV. All structural optimizations were performed using a conjugate-gradient algorithm and a force tolerance criterion for convergence of 0.01 eV/Å. SOC was always included when performing relaxations.

The Mn 3*d*-states were treated employing the GGA+*U* approach⁵² within the Dudarev scheme⁵³. The $U_{\text{eff}} = U - J$ value for the Mn 3*d*-states was chosen to be equal to 5.34 eV, as in previous works²⁴⁻²⁶. Besides, using this U_{eff} we found a good agreement with the HSE06 functional⁵⁴⁻⁵⁶ in the fundamental bandgap and binding energy of the Mn 3*d*-states of bulk MnBi_2Te_4 . Also, we find a very good agreement of the calculated bandgap for the single MnBi_2Te_4 SL block (0.32 eV⁴³) with the measured one (0.35 eV³⁶). Moreover, the indirect character of the gap is correctly reproduced as well. Note that the GGA itself describes the bandgap of a single SL MnBi_2Te_4 film unsatisfactorily both in terms of the character (it yields direct gap) and size (43 meV). Thus, the use of GGA+*U* improves the description of the *p-d* hybridization in the system. Further extensive testing was performed to check the stability of the results against U_{eff} variation. Namely, the bulk crystal structure was fully optimized for different U_{eff} values (3, 4, and 5.34 eV) and then

the magnetic ordering was studied. It was found that the AFM ground state does not change upon such variations of U_{eff} and the crystal structure. The MnBi_2Te_4 magnetic anisotropy was found to be stable against these variations as well.

To model the interlayer AFM structure in MnBi_2Te_4 , we used a rhombohedral cell with 14 atoms. These calculations were performed with the 3D Brillouin zone sampled by a $9 \times 9 \times 9$ k -point grid.

The magnetic anisotropy energy, $E_a = E_{\text{diff}} + E_d$, was calculated taking into account both the total-energy differences of various magnetization directions, $E_{\text{diff}} = E_{\text{in-plane}} - E_{\text{out-of-plane}}$, and the energy of the classical dipole-dipole interaction. To calculate E_{diff} , the energies for three inequivalent magnetization directions [Cartesian x , y (in-plane) and z (out-of-plane)] were calculated and E_{diff} was determined as the difference $E_{\text{in-plane}} - E_z$, where $E_{\text{in-plane}}$ is the energy of the most energetically favorable in-plane direction of the magnetization. A k -mesh of 2197 points was chosen, and the total energies were calculated self-consistently for all considered directions. The calculations of E_{diff} were done for the interlayer AFM state in the cell containing 14 atoms (Fig. 1d). The energy convergence criterion was set to 10^{-7} eV providing a well-converged E_{diff} (up to a few tenths of meV) and excluding “accidental” convergence. A cutoff radius of at least 20 μm was used to calculate E_d .

The Z_2 invariant for the 3D AFMTI was calculated according to Ref. [57]. When spatial inversion symmetry is present in the system, as it is in the MnBi_2Te_4 case, the following Z_2 invariant ζ_0 can be defined:

$$(-1)^{\zeta_0} = \prod_{\mathbf{k}_{\text{inv}} \in B\text{-TRIM}, n \in \text{occ}/2} \zeta_n(\mathbf{k}_{\text{inv}}),$$

where ζ_n is the parity of the n th occupied band. See Ref. [57] for further details.

The MnBi_2Te_4 semi-infinite surface was simulated within a model of repeating films separated by a vacuum gap of a minimum of 10 \AA . A 56-atomic-layers-thick slab was used, which corresponds to 8 SLs. The interlayer distances were optimized for the utmost SL block of each surface. Both the structural optimizations and static electronic structure calculations were performed using a k -point grid of $11 \times 11 \times 1$ in the two-dimensional Brillouin zone.

Exchange coupling constants calculations

For the equilibrium structures obtained with VASP, we calculated the Heisenberg exchange coupling constants $J_{0,j}$ also from first principles, this time using the full-potential linearized augmented plane waves (FLAPW) formalism⁵⁸ as implemented in Fleur⁵⁹. We took the GGA+ U approach^{60,61} under the fully localized limit⁶². For the self-consistent FLAPW basis set in the MnBi_2Te_4 compound we chose a dense $22 \times 22 \times 22$ Monkhorst-Pack k -point sampling of the first Brillouin zone and a cutoff of 3.4 Hartree. The density and potential expansions were cut at 10.4 Hartree. Locally, muffin tin sphere

radii values of 2.74 a.u. for Mn and 2.81 a.u. for Bi and Te atoms were used, and the partial wave functions were expanded up to cutoffs of $l = 8$. Mn, Bi, and Te contribute $4s3d$, $5s5p$, and $6s6p$ valence electrons, respectively. We verified that these settings reproduce with great accuracy the bandstructures obtained with VASP, both with and without SOC effects. The FM vs. AFM ordering energy differences are also in agreement.

The $J_{0,j}$ constants were extracted by Fourier inversion of the magnon energy dispersion for the MnBi_2Te_4 primitive cell^{59,63,64} neglecting SOC. These dispersion energies, calculated in the force theorem approach, correspond to a constrained set of non-collinear spin configurations characterized by the magnon q -vectors of a $13 \times 13 \times 13$ grid^{59,65}. The reference self-consistent electron wave functions were obtained with a $12 \times 12 \times 12$ k -grid. These grids provided magnon energies converged below 0.1 meV and allowed to add up to 150 neighboring atoms to the Fourier analysis, ensuring accurate $J_{0,j}$ values.

Paramagnons calculations

Paramagnetic fluctuations were calculated within a first-principles approach based on the coherent potential approximation⁶⁶⁻⁶⁹. The disordered local moment (DLM) method was used to take ensemble averages over the orientational configurations of the local moments⁷⁰. Paramagnons are calculated considering the response of the DLM paramagnetic state to the application of an external, site-dependent, magnetic field⁷¹.

Ab-initio-based tight-binding calculations

Ab-initio-based tight-binding calculations were performed using the VASP package with the WANNIER90 interface^{72,73}. The wannier basis chosen consisted of six spinor p -type orbitals $|p_x^\uparrow\rangle$, $|p_y^\uparrow\rangle$, $|p_z^\uparrow\rangle$, $|p_x^\downarrow\rangle$, $|p_y^\downarrow\rangle$, $|p_z^\downarrow\rangle$ of Bi and Te. The surface electronic band structure was calculated within the semi-infinite medium Green function approach^{74,75}.

Monte Carlo simulations

The Monte Carlo (MC) simulations were based on a classical Heisenberg Hamiltonian including a magnetic anisotropy energy E_a

$$H = -\frac{1}{2} \sum_{ij} J_{i,j} \mathbf{e}_i \cdot \mathbf{e}_j + \sum_i E_a (\mathbf{e}_i^z)^2,$$

where the magnetic moments at site i and j are described by unit vectors \mathbf{e}_i and \mathbf{e}_j , respectively, and the magnetic coupling constants $J_{i,j}$ are determined by *ab initio* calculations as described above. The term of the magnetic anisotropy takes into account only the z component of the magnetic moment. We created for the simulation of the bulk system a cluster with periodic boundary conditions. Therein, the cluster size was varied with the primitive unit cell repeated N times in all directions with $N = 12, 14, \dots, 20$. This variation of system size allowed us to avoid finite size effects. We have tentatively started the calculation at a temperature of 60 K and reduced T stepwise until 0.001 K. At each temperature step, the thermal equilibrium was reached after 40 000 MC steps (chosen

after comparing results for 20 000 to 100 000 MC steps for all systems). The same number of MC steps was then used to derive the observables after reaching thermal equilibrium. One MC step represents the creation of a new random spin direction, which is either accepted or not depending on the energy difference and the current temperature. The critical temperature was finally obtained from the peak in the magnetic susceptibility, which represented the clearest identification criterion.

Crystal growth

Dresden samples (D samples)

High-quality bulk single crystals of MnBi_2Te_4 were grown from the melt by slow cooling of a 1:1 mixture of the binaries Bi_2Te_3 and $\alpha\text{-MnTe}$. The binaries were synthesized by mechanical pre-activation and annealing of stoichiometric mixtures of the elements. Crystal size and quality were controlled via different cooling rates within a narrow temperature interval at around 600 °C and varying annealing times. Further details of crystal-growth optimization are reported elsewhere⁷⁶. Single-crystal X-ray diffraction was measured on a four-circle Kappa APEX II CCD diffractometer (Bruker) with a graphite(002)-monochromator and a CCD-detector at $T = 296(2)$ K. Mo-K α radiation ($\lambda = 71.073$ pm) was used. A numerical absorption correction based on an optimized crystal description⁷⁷ was applied, and the initial structure solution was performed in JANA2006⁷⁸. The structure was refined in SHELXL against $F_o^{279,80}$. The crystal structure has been deposited in the joint Cambridge Crystallographic Data Centre/FIZ Karlsruhe under the depository number CSD-1867581. The structure refinement yields some degree of statistical cation disorder in the Mn and Bi positions in contrast to an earlier reported ordered model¹¹. Mn/Bi antisite defects in two fully occupied cation positions do not, however, lead to a superstructure ordering or change of translational symmetry. Energy dispersive X-ray spectra (EDS) were collected using an Oxford Silicon Drift X-MaxN detector at an acceleration voltage of 20 kV and a 100 s accumulation time. The analysis was performed using the $P/B - ZAF$ standardless method (where Z = atomic no. correction factor, A = absorption correction factor, F = fluorescence factor, and P/B = peak to background model). EDS reproducibly results in the stoichiometric composition, ruling out a possibility of large compositional variations in our samples.

Baku samples (B samples)

The bulk ingot of the Baku sample was grown from the melt with a non-stoichiometric composition using the vertical Bridgman method. The pre-synthesized polycrystalline sample was evacuated in a conical-bottom quartz ampoule sealed under vacuum better than 10^{-4} Pa. In order to avoid the reaction of the manganese content of the sample with the silica container during the melting process, the inside wall of the ampoule was coated with graphite by thermal decomposition of acetone in an oxygen-poor environment. The ampoule was held in the “hot” zone (~ 680 °C) of a two-zone tube furnace of the MnBi_2Te_4 Bridgman crystal growth system for 8 h to achieve a complete homogenization of the

melts. Then, it moved from the upper (hot) zone to the bottom (cold) zone with the required rate of 0.7 mm/h. Consequently, the bulk ingot with average dimensions of 3 cm in length and 0.8 cm in diameter was obtained. Further details are reported elsewhere⁸¹. The as-grown ingot was checked by X-ray diffraction (XRD) measurements and was found to consist of several single crystalline blocks. With the aid of XRD data high quality single crystalline pieces were isolated from different parts of the as-grown ingot for further measurements.

Magnetic measurements

The magnetic measurements as a function of temperature and magnetic field were performed on a stack of single crystals of MnBi_2Te_4 (D samples) using a SQUID (Superconducting Quantum Interference Device) VSM (Vibrating Sample Magnetometer) from Quantum Design. The temperature dependent magnetization measurements were acquired in external magnetic fields of 0.02 T and 1 T for both zero-field-cooled (zfc) and field-cooled-warming (fcw) conditions. A thorough background subtraction was performed for all the curves.

Part of the magnetic measurements were carried out in the resource center “Center for Diagnostics of Materials for Medicine, Pharmacology and Nanoelectronics” of the SPbU Science Park using a SQUID magnetometer with a helium cryostat manufactured by Quantum Design. The measurements were carried out in a pull mode in terms of temperature and magnetic field. The applied magnetic field was perpendicular to the (0001) sample surface.

Resistivity measurements

Resistivity measurements were done with a standard four-probe ac technique using a low-frequency ($f \sim 20$ Hz) lock-in amplifier. Contacts were attached with conducting graphite paste. The measurements were carried out in a temperature-variable cryostat at different values of magnetic field up to 8 T, generated by a superconducting solenoid and directed along the normal to the (0001) sample surface.

Temperature- and field-dependent resistivity measurements were performed on B samples (Extended Data Fig. 3a). The metallic-like behavior characteristic of the presence of free carriers is observed at $H = 0$ as the resistivity ρ increases with rising temperature. This is consistent with the results of the Hall effect measurements yielding the n -type conductivity of these samples (Extended Data Fig. 3b). A well-defined kink at 25.4 K indicates a magnetic transition in agreement with the magnetization studies and Monte Carlo simulations. In a series of measurements under an external field $H \perp (0001)$ the kink shifts to lower temperatures as the field increases from 1 T to 3 T. Above the critical field of ~ 3 T to 4 T, the $\rho(T)$ curve slope is much steeper below T_N , which could be related to the observed spin-flop in the $M(H)$ curve (Fig. 2d).

ESR measurements

ESR experiments were performed with a commercial X-band ESR-spectrometer (EMX from Bruker) operating at a microwave frequency of 9.6 GHz and providing magnetic fields up to 0.9 T. It is equipped with a He-gas flow cryostat (Oxford Instruments) and a goniometer allowing temperature and angular dependent measurements between 4 and 300 K.

The temperature dependence of the resonance field H_{res} of the ESR signal of Mn^{2+} ions in $MnBi_2Te_4$ is measured for the out-of-plane $H \perp (0001)$ and in-plane $H \parallel (0001)$ orientations of the static magnetic field H . At high temperatures H_{res} is practically isotropic within the error bars and the corresponding spectroscopic g -factor is very close to the spin-only value $g_s = 2$ as expected for the Mn^{2+} ($3d^5$; $S = 5/2$; $L = 0$) ion⁸². However, below $T \sim 50$ K H_{res} becomes anisotropic and, in particular, the resonance line rapidly shifts to smaller fields for the out-of-plane geometry indicating an onset of the quasi-static short-range magnetic correlations developing in $MnBi_2Te_4$ well above the AFM phase transition at T_N . By further lowering the temperature, the linewidth experiences critical broadening due to the slowing down of the spin fluctuations in the vicinity of T_N ⁸³ (Fig. 4a). Finally, upon entering the AFM ordered state the intensity of the ESR signal rapidly decreases, because of the shifting of the spectral weight to the AFM collective resonance modes typically occurring at much higher frequencies than the paramagnetic resonance⁸⁴ and, thus, out of the frequency range of the used ESR setup. Observation of quasi-static short-range magnetic correlations in the ESR experiment is consistent with the strong spin fluctuation-driven spin scattering above T_N found in the magneto-transport study of $MnBi_2Te_4$ in Ref. [37].

ARPES measurements

The ARPES experiments were carried out at the BaDElPh beamline⁸⁵ of the Elettra synchrotron in Trieste (Italy) and BL-1 of the Hiroshima synchrotron radiation center (Japan) using p -polarization of the synchrotron radiation and laser^{86,87}. The photoemission spectra were collected on freshly cleaved surfaces. The base pressure during the experiments was better than 1×10^{-10} mbar. Part of the ARPES experiments were also carried out in the resource center “Physical methods of surface investigation” (PMSI) at the Research park of Saint Petersburg State University.

Additional $h\nu$ -dependent experiments on D samples (the data are shown in Extended Data Fig. 7) were performed at the MAESTRO endstation of the Advanced Light Source (ALS).

Dichroic ARPES measurements

The linear-dichroism ARPES measurements on D samples (Extended Data Fig. 8) were performed at the MAESTRO endstation of the Advanced Light Source (ALS). This kind of measurement allow us to explore influence of the AFM state on the wave function of the topological surface state (TSS). With p -polarized light incident in the xz -plane the linear dichroism (LD) in the photoelectron intensity can be defined as⁸⁸⁻⁹¹:

$$LD(k_x, k_y, E) = I(k_x, k_y, E) - I(-k_x, k_y, E).$$

The LD is the intensity asymmetry relative to the yz -plane. In the present experiment the yz -plane is a crystalline mirror plane. Therefore, in the absence of a magnetization, the LD is induced by the mirror-symmetry breaking of the light electric field vector $\mathcal{E} = (\mathcal{E}_x, 0, \mathcal{E}_z)$. The intensities along $\pm k_x$ can be written as $I(\pm k_x) = |T_z \pm T_x|^2$, where T_z and T_x are the photoemission matrix elements of the electric field components \mathcal{E}_z and \mathcal{E}_x between the photoelectron final state Φ_f and the initial state ψ_i at a given k_x ⁸⁸. One then finds $LD = 4\Re(T_z^* T_x)$, implying that a change of either matrix element will also change the LD. In particular, a change of the TSS wave function across T_N , will manifest in the LD because the TSS enters the matrix elements as the initial-state wave function ψ_i . This is precisely what we observe in Extended Data Fig. 8a,b,c: at temperatures above T_N an LD is already present, but it gets considerably enhanced below T_N . This effect is understood as the effect of the AFM order on ψ_i . In the present case, as described in the main manuscript, T_N marks the transition between the AFM state and a paramagnetic state with anisotropic fluctuations. Our LD-measurements provide strong evidence for an effect of the AFM order on the TSS wave function.

Our theoretical calculations provide additional insight into the origin of the LD. The crystal structure of the (0001) surface of MnBi_2Te_4 has 3 mirror planes along the $\bar{\Gamma} - \bar{M}$ directions of the 2D BZ. In the nonmagnetic case, the presence of these mirror planes dictates that the out-of-plane spin components are zero for the $\bar{\Gamma} - \bar{M}$ directions, along which the spins are locked exclusively within the surface plane. However, for the $\bar{\Gamma} - \bar{K}$ directions the s_z components are allowed by symmetry and therefore can coexist with the in-plane spins. As one can see in Ref. [24], in the case of an isostructural compound GeBi_2Te_4 *ab initio* calculations indeed reveal the presence (absence) of the out-of-plane spins for the $\bar{\Gamma} - \bar{K}$ ($\bar{\Gamma} - \bar{M}$) directions. At $\text{GeBi}_2\text{Te}_4(0001)$, the out-of-plane spin components are especially pronounced out of the fundamental bandgap energy region, where the TSS coincides with the bulk states in energy (but not in k_{\parallel}). By analogy, the appearance of the out-of-plane spin components along $\bar{\Gamma} - \bar{K}$ can be expected for the TSS of $\text{MnBi}_2\text{Te}_4(0001)$. Such a spin texture is required to respect the time-reversal symmetry if the AFM exchange field inherent to the material is artificially set to zero. In this case, the s_z sign will change upon changing $+k_{\parallel}$ (right branch) to $-k_{\parallel}$ (left branch). When the time-reversal symmetry is broken and each MnBi_2Te_4 SL is ferromagnetically ordered, the right and left branches of the TSS interact differently with the Zeeman field provided by the Mn layer of the topmost SL block (Extended Data Fig. 8d). This is similar to a so-called exchange+Rashba effect^{92,93}. In such cases, a dispersion asymmetry is created (i.e. $E(+k_{\parallel}) \neq E(-k_{\parallel})$), which is indeed seen for the MnBi_2Te_4 TSS (Extended Data Fig. 8d,e), resulting in a sizable asymmetry in the orbital composition between its right and left branches (Extended Data Fig. 8e,f). Note that such asymmetries are not found in our calculations for the $\bar{\Gamma} - \bar{M}$ directions because of the symmetry constraints on the presence of s_z components in the time-reversal symmetry preserving case. In the time-reversal symmetry breaking case, the s_z components appear along the $\bar{\Gamma} - \bar{M}$ directions, which also breaks the mirror symmetry at the $\text{MnBi}_2\text{Te}_4(0001)$ surface.

Temperature-dependent laser ARPES measurements

To study the Dirac cone state response to the onset of the AFM order, we carried out the temperature-dependent high-resolution laser ARPES measurements for the $\text{MnBi}_2\text{Te}_4(0001)$ surface. In Extended Data Fig. 9a, the raw EDC profiles at the $\bar{\Gamma}$ -point at 10.5 and 35 K are presented (the same as in Figs. 3g,h of the manuscript), clearly showing the increase of the intensities of both the upper and lower parts of the Dirac cone state below the Néel temperature. Before studying the Dirac cone intensity variation systematically, we have carefully analyzed the intensity of the first two bulk conduction band states (those shown in the Extended Data Fig. 5c). No temperature dependence of the integral intensity of these bulk states was observed (Extended Data Fig. 9b) and therefore the EDC spectra require no specific temperature-dependent normalization. Thus, the intensity temperature dependence was obtained using the raw ARPES data. The results are shown in Extended Data Fig. 9c. Here, the $\bar{\Gamma}$ -point EDC profiles, acquired with a step of ~ 0.9 K, are plotted versus temperature. Below ~ 24 -25 K, the intensity enhancement in the $\Delta E = [0.2; 0.3]$ eV energy window, containing the Dirac cone state at the $\bar{\Gamma}$ -point, is clearly seen. Note that these temperature-dependent ARPES spectra were measured with the equal acquisition time and the constant laser photon flux for each temperature point in Extended Data Fig. 9c. In order to get deeper insight into this behavior of intensity, we integrate it within the energy window ΔE and plot as a function of temperature in Extended Data Fig. 9d (the same data are presented in Fig. 3e of the manuscript). It is seen that while the Dirac cone intensity is roughly constant above $T_N \approx 24$ K, below the Néel temperature it starts to grow and at 10 K gets enhanced by a factor of 1.4-1.5 as compared to its value at 35 K.

It should be noted that during the ARPES measurements the spectra acquisition time is rather limited, which is due to a finite “lifetime” of the clean surface of the sample even under the ultrahigh vacuum conditions. This lifetime is well comparable to the time needed to acquire several high quality ARPES maps (such as shown in Figs. 3g,h), that are suitable for a reliable comparative EDC spectral analysis (fitting). However, within the lifetime of the clean surface of the sample, such a long acquisition time per temperature point is unreachable during the systematic temperature-dependent measurements that in our case are made with more than 50 temperature points, i.e. $\Delta T \approx 0.9$ K and two sweep directions (10 K \rightarrow 35 K \rightarrow 10 K). Although the measured EDCs shown in Extended Data Fig. 9c are obviously meaningful, their spectral decomposition (fitting), similar to that shown in Extended Data Fig. 9a, is not unambiguous. Treated without any normalization, these raw data clearly show a strong intensity change across the Néel temperature.

As it can be seen from the EDC analysis (Extended Data Fig. 9a), the intensity increase observed is largely due to the enhancement of the gapped Dirac cone peaks intensities, while the signal between those peaks (i.e. within the DP gap) is practically the same for 10.5 and 35 K. Therefore, at 35 K the intensity inside the DP gap increases *relative* to those of the Dirac cone peaks, indicative of an enhancement of the spectral weight inside the gap. The temperature-dependent change of the line shape around the DP gap can be

nicely demonstrated by the behavior of the second derivative ($d^2N(E)/dE^2$), which is highly sensitive to the curvature of the spectrum $N(E)$, see Extended Data Fig. 9e. Indeed, at low temperatures one can see a pronounced feature of the second derivative around the binding energy of 0.25 eV, signaling the presence of the DP gap, while above the Néel temperature this feature is significantly weaker. These changes clearly demonstrate the gapped state mitigation across the antiferromagnet-paramagnet transition.

Spin-ARPES measurements

Spin-resolved ARPES measurements were performed at the RGBL-2 endstation of BESSY-II in Berlin using a Scienta R4000 hemispherical analyzer and a photon energy of 6 eV. The photon beam was generated using the fourth harmonic of a homemade fs-laser system coupled to an ultrafast amplifier operating at 100 kHz repetition rate. The spin-resolved spectra were acquired with a 3D Mott-type spin detector operated at 26 kV. We used the vertical linearly polarized light incident on the sample under an angle of 45° with respect to the surface normal. The experimental geometry is given in Ref. [94]. The energy and angular resolutions of the spin-resolved measurements were 30 meV and 1.5° (corresponds to 0.02 \AA^{-1}), respectively.

ResPES measurements

ResPES data were acquired at the HR-ARPES branch of the I05 beamline at the Diamond Light Source. The measurements were conducted at a base temperature of $T = 10 \text{ K}$ with a beam spot size and energy resolution of $A_{\text{spot}} \approx 50 \times 50 \text{ \mu m}^2$ and $E \approx 20 \text{ meV}$, respectively. The difference of on- and off-resonant spectra for the Mn $3p-3d$ transition corresponds directly to the Mn $3d$ density of states. A photon energy series was conducted in order to determine suitable transition energies. The corresponding angle integrated spectra of on-resonant ($h\nu = 51 \text{ eV}$) and off-resonant ($h\nu = 47 \text{ eV}$) conditions can be seen in Fig. 3i.

XMCD measurements

Surface sensitive XMCD measurements (TEY mode⁹⁵) on D samples were performed at the HECTOR end-station of the BOREAS beamline at the ALBA synchrotron radiation facility⁹⁶. The data were collected in total electron yield mode. The spot size and the resolving power of the supplied photon beam were $A_{\text{spot}} < 200 \times 200 \text{ \mu m}^2$ and $E/\Delta E > 9000$, respectively. Measurements were performed at the Mn- $L_{2/3}$ edges at a temperature of 2 K, i.e. well below $T_N \approx 24 \text{ K}$.

44. Blöchl, P. E. Projector augmented-wave method. Phys. Rev. B **50**, 17953-17979 (1994).
45. Kresse, G. & Furthmüller, J. Efficient iterative schemes for *ab initio* total-energy calculations using a plane-wave basis set. Phys. Rev. B **54**, 11169-11186 (1996).
46. Kresse, G. & Joubert, D. From ultrasoft pseudopotentials to the projector augmented-wave method. Phys. Rev. B **59**, 1758-1775 (1999).

47. Perdew, J. P., Burke, K. & Ernzerhof, M. Generalized gradient approximation made simple. *Phys. Rev. Lett.* **77**, 3865-3868 (1996).
48. Koelling, D. D. & Harmon, B. N. A technique for relativistic spin-polarised calculations. *J. Phys. C: Sol. St. Phys.* **10**, 3107 (1977).
49. Grimme, S. Semiempirical GGA-type density functional constructed with a long-range dispersion correction. *J. Comput. Chem.* **27**, 1787-1799 (2006).
50. Grimme, S., Antony, J., Ehrlich, S. & Krieg, H. A consistent and accurate *ab initio* parametrization of density functional dispersion correction (DFT-D) for the 94 elements H-Pu. *J. Chem. Phys.* **132**, 154104 (2010).
51. Grimme, S., Ehrlich, S. & Goerigk, L. Effect of the damping function in dispersion corrected density functional theory. *J. Comput. Chem.* **32**, 1456-1465 (2011).
52. Anisimov, V. I., Zaanen, J. & Andersen, O. K. Band theory and Mott insulators: Hubbard U instead of Stoner I . *Phys. Rev. B* **44**, 943-954 (1991).
53. Dudarev, S. L., Botton, G. A., Savrasov, S. Y., Humphreys, C. J. & Sutton, A. P. Electron-energy-loss spectra and the structural stability of nickel oxide: An LSDA+ U study. *Phys. Rev. B* **57**, 1505-1509 (1998).
54. Becke, A. D. Density-functional exchange-energy approximation with correct asymptotic behavior. *Phys. Rev. A* **38**, 3098 (1988).
55. Perdew, J. P., Ernzerhof, M. & Burke, K. Rationale for mixing exact exchange with density functional approximations. *J. Chem. Phys.* **105**, 9982-9985 (1996).
56. Heyd, J., Scuseria, G. E. & Ernzerhof, M. Hybrid functionals based on a screened Coulomb potential. *J. Chem. Phys.* **118**, 8207-8215 (2003).
57. Fang, C., Gilbert, M. J. & Bernevig, B. A. Topological insulators with commensurate antiferromagnetism. *Phys. Rev. B* **88**, 085406 (2013).
58. Wimmer, E., Krakauer, H., Weinert, M. & Freeman, A. J. Full-potential self-consistent linearized-augmented-plane-wave-method for calculating the electronic structure of molecules and surfaces: O_2 molecule. *Phys. Rev. B* **24**, 864-875 (1981).
59. Fleur site: <http://www.flapw.de>.
60. Anisimov, V. I., Aryasetiawan, F. & Lichtenstein, A. I. First-principles calculations of the electronic structure and spectra of strongly correlated systems: the LDA+ U method. *Journal of Physics: Condensed Matter* **9**, 767 (1997).
61. Shick, A. B., Lichtenstein, A. I. & Pickett, W. E. Implementation of the LDA+ U method using the full-potential linearized augmented plane-wave basis. *Phys. Rev. B* **60**, 10763-10769 (1999).
62. Anisimov, V. I., Solovyev, I. V., Korotin, M. A., Czyżyk, M. T. & Sawatzky, G. A. Density-functional theory and NiO photoemission spectra. *Phys. Rev. B* **48**, 16929-16934 (1993).
63. Sandratskii, L. M. & Bruno, P. Exchange interactions and Curie temperature in (Ga,Mn)As. *Phys. Rev. B* **66**, 134435 (2002).
64. Ležaić, M., Mavropoulos, P., Enkovaara, J., Bihlmayer, G. & Blügel, S. Thermal collapse of spin polarization in half-metallic ferromagnets. *Phys. Rev. Lett.* **97**, 026404 (2006).

65. Kurz, P., Förster, F., Nordström, L., Bihlmayer, G. & Blügel, S. *Ab initio* treatment of noncollinear magnets with the full-potential linearized augmented plane wave method. *Phys. Rev. B* **69**, 024415 (2004).
66. Soven, P. Coherent-Potential Model of Substitutional Disordered Alloys. *Phys. Rev.* **156**, 809 (1967).
67. Gyorffy, B. L. Coherent-Potential Approximation for a Nonoverlapping-Muffin-Tin-Potential Model of Random Substitutional Alloys. *Phys. Rev. B* **5**, 2382 (1972).
68. Lüders, M., Ernst, A., Temmerman, W. M., Szotek, Z. & Durham, P. J. *Ab initio* angle-resolved photoemission in multiple-scattering formulation. *J. Phys.: Condens. Matter* **13**, 8587 (2001).
69. Geilhufe, M., Achilles, S., Köbis, M. A., Arnold, M., Mertig, I., Hergert, W., Ernst, A. Numerical solution of the relativistic single-site scattering problem for the Coulomb and the Mathieu potential. *J. Phys.: Condens. Matter* **27**, 435202 (2015).
70. Gyorffy, B. L., Pindor, A. J., Staunton, J., Stocks, G. M. & Winter, H. A first-principles theory of ferromagnetic phase transitions in metals. *Journal of Physics F: Metal Physics* **15**, 1337 (1985).
71. Staunton, J., Gyorffy, B. L., Pindor, A. J., Stocks, G. M. & Winter, H. Electronic structure of metallic ferromagnets above the Curie temperature. *Journal of Physics F: Metal Physics* **15**, 1387 (1985).
72. Marzari, N., & Vanderbilt, D. Maximally localized generalized Wannier functions for composite energy bands. *Phys. Rev. B* **56**, 12847 (1997).
73. Mostofi, A. A., Yates, J. R., Lee, Y.-S., Souza, I., Vanderbilt, D. & Marzari, N. wannier90: A tool for obtaining maximally-localized Wannier functions. *Computer Physics Communications* **178**, 685-699 (2008).
74. Lopez Sancho, M. P., Lopez Sancho, J. M., Sancho, J. M. L., & Rubio, J. Highly convergent schemes for the calculation of bulk and surface Green functions. *Journal of Physics F: Metal Physics* **15**, 851-858 (1985).
75. Henk, J., & Schattke, W. A subroutine package for computing Green's functions of relaxed surfaces by the renormalization method. *Computer Physics Communications* **77**, 69-83 (1993).
76. Zeugner, A. et al. Chemical Aspects of the Candidate Antiferromagnetic Topological Insulator MnBi_2Te_4 . *Chem. Mater.* **31**, 2795-2806 (2019).
77. X-Shape, Crystal Optimization for Numerical Absorption Correction Program. v. 2.12.2, Stoe & Cie GmbH, Darmstadt, 2009.
78. Petricek, V., Dusek, M. & Palatinus, L. JANA2006, The Crystallographic Computing System (Institute of Physics, Praha, Czech Republic, 2011).
79. Sheldrick, G. M. SHELXL, Program for Crystal Structure Refinement Multi-CPU v. 2014/7 (Georg-August-Universität Göttingen, Göttingen, Germany, 2014).
80. Sheldrick, G. M. A short history of SHELX. *Acta Cryst. A* **64**, 112-122 (2008).
81. Aliev, Z. S., Amiraslanov, I. R., Nasonova, D. I., Shevelkov, A. V., Abdullayev, N. A., Jahangirli, Z. A., Orujlu, E. N. et al. Novel ternary layered manganese

- bismuth tellurides of the MnTe-Bi₂Te₃ system: Synthesis and crystal structure. *J. Alloys Compd.* **789**, 443-450 (2019).
82. Abragam, A. & Bleaney, B. *Electron Paramagnetic Resonance of Transition Ions*. International Series of Monographs on Physics (Oxford University, New York, 2012).
 83. Benner, H. & Boucher, J. *Magnetic properties of layered transition metal compounds* (Kluwer academic publishers, Dordrecht, Boston, London, 1990).
 84. Turov, E. A. *Physical Properties of Magnetically Ordered Crystals* (Academic Press, New York, 1965).
 85. Petaccia, L. et al. BaD EIPh: A 4 m normal-incidence monochromator beamline at Elettra. *Nucl. Instrum. Methods Phys. Res. A* **606**, 780-784 (2010).
 86. Iwasawa, H. et al. Rotatable high-resolution ARPES system for tunable linear-polarization geometry. *J. Synchrotron Rad.* **24**, 836-841 (2017).
 87. Iwasawa, H. et al. Development of laser-based scanning μ -ARPES system with ultimate energy and momentum resolutions. *Ultramicroscopy* **182**, 85-91 (2017).
 88. Bentmann, H. et al. Strong Linear Dichroism in Spin-Polarized Photoemission from Spin-Orbit-Coupled Surface States. *Phys. Rev. Lett.* **119**, 106401 (2017).
 89. S.V. Chernov and K. Medjanik and C. Tusche and D. Kutnyakhov and S.A. Nepijko and A. Oelsner and J. Braun and J. Minar and S. Borek and H. Ebert and H.J. Elmers and J. Kirschner and G. Schönhense. Anomalous *d*-like surface resonances on Mo(110) analyzed by time-of-flight momentum microscopy. *Ultramicroscopy* **159**, 453-463 (2015).
 90. Tusche, C. et al. Multi-mhz time-of-flight electronic bandstructure imaging of graphene on Ir(111). *Applied Physics Letters* **108**, 261602 (2016).
 91. Schönhense, G. et al. Spin-filtered time-of-flight *k*-space microscopy of Ir towards the complete photoemission experiment. *Ultramicroscopy* **183**, 19-29 (2017).
 92. Krupin, O. et al. Rashba effect at magnetic metal surfaces. *Phys. Rev. B* **71**, 201403 (2005).
 93. Rybkin, A. G. et al. Magneto-Spin-Orbit Graphene: Interplay between Exchange and Spin-Orbit Couplings. *Nano Lett.* **18**, 1564-1574 (2018).
 94. Sánchez-Barriga, J., Battiato, M., Krivenkov, M., Golias, E., Varykhalov, A., Romualdi, A., Yashina, L. V., Minár, J., Kornilov, O., Ebert, H., Held, K., & Braun, J. *Phys. Rev. B* **95**, 125405 (2017).
 95. Abbate, M. et al. Probing depth of soft X-ray absorption spectroscopy measured in total-electron-yield mode. *Surf. Interface Anal.* **18**, 65-69 (1992).
 96. Barla, A. et al. Design and performance of BOREAS, the beamline for resonant X-ray absorption and scattering experiments at the ALBA synchrotron light source. *J. Synchrotron Rad.* **23**, 1507-1517 (2016).

Data availability

The data that support the findings of this study are available from the corresponding author upon reasonable request. The crystal structure is available in the joint Cambridge Crystallographic Data Centre/FIZ Karlsruhe under the depository number CSD-1867581.

Extended Data figure legends

Extended Data Figure 1. Monte Carlo simulations for bulk MnBi₂Te₄. The temperature dependent-magnetic susceptibility of bulk MnBi₂Te₄ calculated for various numbers of magnetic shells j up to which the exchange coupling constants $J_{i,j}$ were considered in the classical Heisenberg Hamiltonian. Up to 10, 20, ... 70 shells were included in the calculation. The vertical dashed line shows the final Néel temperature of 25.4 K as estimated for the calculation including 70 shells. Note that only above 20 shells, the Monte Carlo simulations determined the antiferromagnetic ground state.

Extended Data Figure 2. Electronic structure of the S -breaking and S -preserving surfaces of MnBi₂Te₄. Surface electronic bandstructure of MnBi₂Te₄ calculated for the (0001), **a** (S -breaking), and (10 $\bar{1}$ 1), **b** (S -preserving), terminations using the *ab-initio*-based tight-binding approach. The regions with a continuous spectrum correspond to the 3D bulk states projected onto a 2D Brillouin zone.

Extended Data Figure 3. Resistivity and Hall measurements of bulk MnBi₂Te₄. **a**, Temperature- and field-dependent resistivity data. **b**, Hall voltage as a function of the applied magnetic field for MnBi₂Te₄ at 5 K. The Hall effect measurements unambiguously indicate the n -type conductivity of our MnBi₂Te₄ samples that show a negative Hall voltage for positive values of the applied magnetic field. The estimated electron concentration and Hall mobility are $\sim 2 \times 10^{19} \text{ cm}^{-3}$ and $\sim 100 \text{ cm}^2/(\text{V}\cdot\text{s})$, respectively. The measurements were performed on B samples.

Extended Data Figure 4. D sample ARPES. **a**, Dispersion of MnBi₂Te₄(0001) measured at 12 K with a photon energy of 28 eV and, **b**, EDC representation of the data shown in **a**. The red curve marks the EDC at the $\bar{\Gamma}$ -point. **c**, ARPES image acquired at 300 K ($h\nu = 28 \text{ eV}$). **d**, Dispersion of MnBi₂Te₄(0001) measured at a temperature of 12 K with a photon energy of 9 eV (which is more bulk sensitive) and, **e**, the corresponding second derivative, $d^2N(E)/dE^2$. **f**, ARPES image acquired at 300 K ($h\nu = 9 \text{ eV}$). The measurements were performed on D samples.

Extended Data Figure 5. Laser-based ARPES. **a**, ARPES map of MnBi₂Te₄ taken at 10 K with a photon energy of 6.3 eV. In this case, the photoelectrons have a kinetic energy of about 1.5 eV and, subsequently, a large mean free path in the sample, corresponding to a high bulk sensitivity of this experiment. **b**, second derivative $d^2N(E)/dE^2$ of the data shown in **a**. **c**, fitting results for the EDC spectrum at the $\bar{\Gamma}$ -point. The raw data, resulting fitting curve and its decomposition with Voigt peaks are shown by blue symbols, black solid line and grey dashed/red solid lines, respectively. Red (grey) lines indicate the peaks attributed to the gapped Dirac cone state (bulk bands). The measurements were performed on B samples.

Extended Data Figure 6. Surface electronic structure of MnBi₂Te₄ in the artificial topologically-trivial phase. Septuple-layer resolved (0001) surface electronic structure of MnBi₂Te₄ calculated for the SOC constant value $\lambda = 0.55\lambda_0$. The size of the color circles reflects the state localization in a particular SL block of the 8-SL-thick slab: **a**, 1st

(i.e. surface; red), **b**, 2nd (subsurface; blue), **c**, 3rd (bulk-like; green), and **d**, 4th (bulk-like; black). The grey areas correspond to the bulk bandstructure projected onto the surface Brillouin zone. It is seen that near the $\bar{\Gamma}$ -point there are (i) no surface states in the bulk bandgap and (ii) no resonance states near the bandgap edges. The first quantum well states of both the valence and conduction bands are strongly localized in the inner parts of the slab.

Extended Data Figure 7. Photon-energy-dependent ARPES data. Photon-energy-dependent ARPES data measured near the Brillouin zone center along the $\bar{K} - \bar{\Gamma} - \bar{K}$ direction at a temperature of 18 K. Absence of $h\nu$ -dependence confirms surface-state character of the upper cone. The measurements were performed on D samples.

Extended Data Figure 8. Temperature-dependent linear dichroism in the Dirac cone photoemission intensity. **a**, Dispersion of $\text{MnBi}_2\text{Te}_4(0001)$ measured at 18 K with a photon energy of 21.5 eV and p -polarized light along the $\bar{K} - \bar{\Gamma} - \bar{K}$ direction. **b**, Momentum distribution curves representation of the data acquired at 18 K (blue) and 80 K (red). **c**, Linear dichroism ($I_{right} - I_{left}$), where I_{right} and I_{left} are the intensities of the right and left branches of the upper and lower cone corresponding to the positive and negative $k_{||}$, respectively. The measurements were performed on D samples. **d**, Upper part of the $\text{MnBi}_2\text{Te}_4(0001)$ gapped Dirac cone as calculated *ab initio*. The size of color circles reflects the value and sign of the spin vector Cartesian projections, with red/blue colors corresponding to the positive/negative s_y components (perpendicular to $k_{||}$), and gold/cyan to the out-of-plane components $+s_z/-s_z$. **e**, The same as in **d**, but with the size of the purple circles reflecting the weight of the p_x -orbitals of all Bi and Te atoms of the topmost SL block at each $k_{||}$. Note that in **d,e** the bulk-like bands of the slab are omitted. The magnetic moment of the topmost Mn layer points towards vacuum, while in Fig. 1f of the manuscript and Extended Data Fig. 6 it points in the opposite direction. **f**, The weight of the s , p_x , p_y , and p_z orbitals of all Bi and Te atoms of the topmost SL block for the left (triangles) and right (squares) branches as a function of energy. See Methods section for more information on the dichroic ARPES measurements.

Extended Data Figure 9. Temperature-dependent laser ARPES measurements. **a**, ARPES EDC profiles taken at the $\bar{\Gamma}$ -point of $\text{MnBi}_2\text{Te}_4(0001)$ at 10.5 and 35 K. The raw data, resulting fitted curves, and their decompositions with Voigt peaks are shown by color symbols, black dashed lines, and color lines/gray symbols, respectively. Red/blue lines (circles/squares) indicate the peaks (EDCs) of the Dirac cone state at 35/10.5 K. The peaks of the bulk bands at 35/10.5 K are shown by gray circles/squares. **b**, Integrated intensity of the first two bulk conduction band states (those analyzed in detail in the Extended Data Fig. 5c) as a function of temperature. The inset shows the ARPES $\text{MnBi}_2\text{Te}_4(0001)$ map measured with laser photon energy of 6.4 eV and $T = 10.5$ K (the same as in Fig. 3f). The green rectangle marks the region of the map where the first two bulk conduction band states are located. The average intensity in the shown temperature interval was set to 1. **c**, EDC profiles, $N(E)$, taken at the $\bar{\Gamma}$ -point between 10 and 35 K with a temperature step ΔT of ~ 0.9 K and two sweep directions (10 K \rightarrow 35 K \rightarrow 10 K). Since the measurements upon heating and cooling reveal essentially the same behavior,

in panel **c** we show the data averaged over these two sets of the EDC profiles at each temperature point. Note that the data in panel **a** and temperature intensity dependencies in panels **b,c,d** were acquired from two different samples, showing slightly different binding energy of the DP gap centers (0.28 vs 0.25 eV, respectively). **d**, Intensity integrated within the energy window ΔE marked by the dashed black lines in **c**. The average intensity in the “plateau-like” region above ~ 24 K was set to 1. ΔE contains both lower and upper parts of the Dirac cone at the $\bar{\Gamma}$ -point and corresponds to the energy interval where the contribution of the cone is dominant, while that of the bulk states is almost negligible. The vertical cyan line approximately shows the start of the intensity increase, which roughly corresponds to $T_N \approx 24$ K of MnBi_2Te_4 . **e**, The second derivative, $d^2N(E)/dE^2$, of the EDC profiles on **c**, shown for better visualization of the DP gap behavior.

Extended Data Figure 10. Spin-resolved ARPES data. **a**, Spin-integrated ARPES spectrum taken at 6 eV photon energy along the $\bar{K} - \bar{\Gamma} - \bar{K}$ direction. Yellow and cyan curves show the location of the gapped topological surface state; **b**, Spin-resolved ARPES spectra taken at the $\bar{\Gamma}$ -point with respect to the out-of-plane spin quantization axis. The out-of-plane spin polarization is shown below the corresponding spin-up and spin-down spectra; **c,d**, Measured out-of-plane and in-plane spin polarization at different momentum values, respectively. The in-plane spin polarization changes its sign with k_{\parallel} , as expected for the topological surface state. The change of the out-of-plane spin polarization sign at $k_{\parallel} = +0.1 \text{ \AA}^{-1}$ near the Fermi level in panel **c** is discussed in the Methods section dedicated to the dichroic ARPES measurements description. The data on **a,b** and **c,d** were acquired on B and D samples, respectively. The measurements were performed at $T = 300$ K.

Figure 1

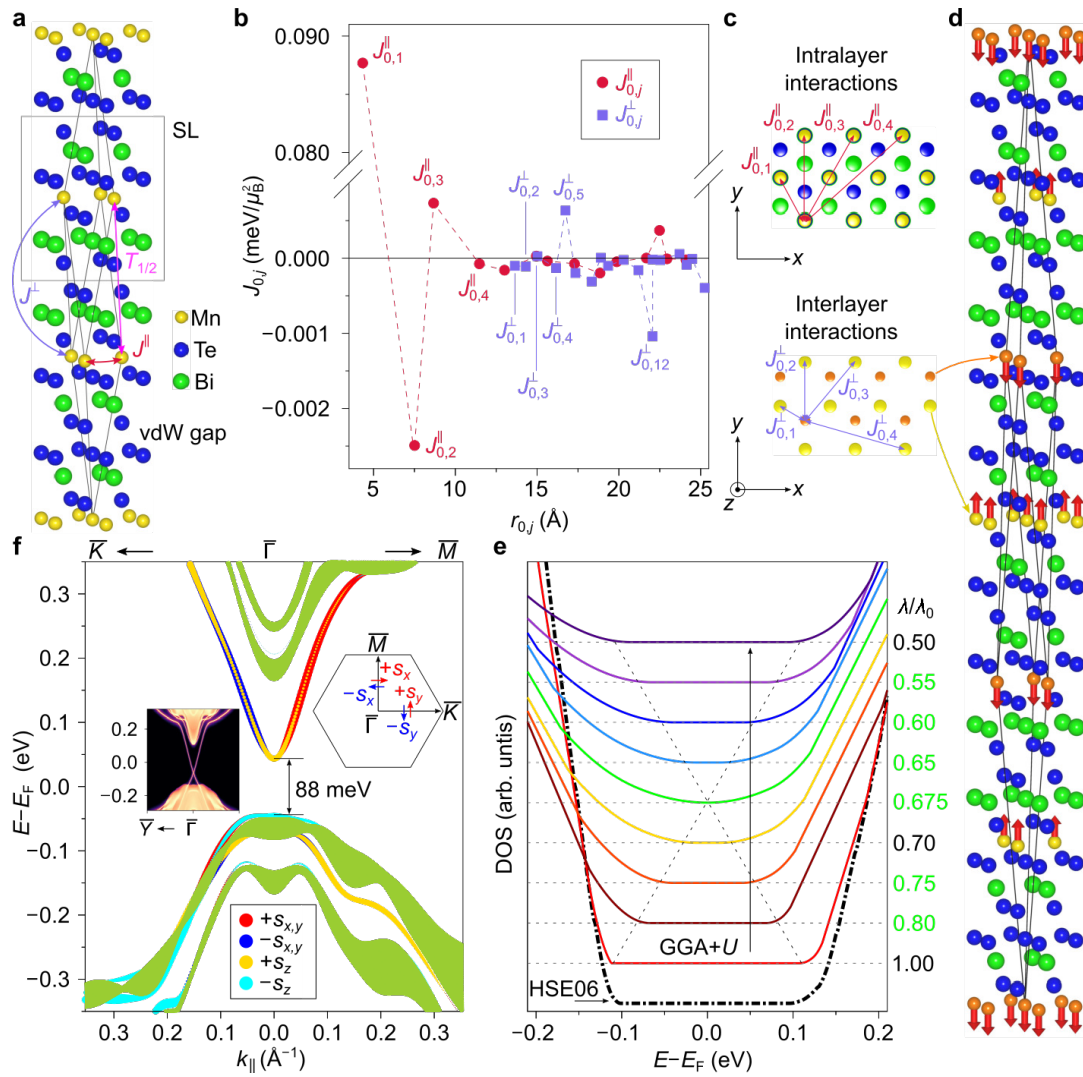


Figure 2

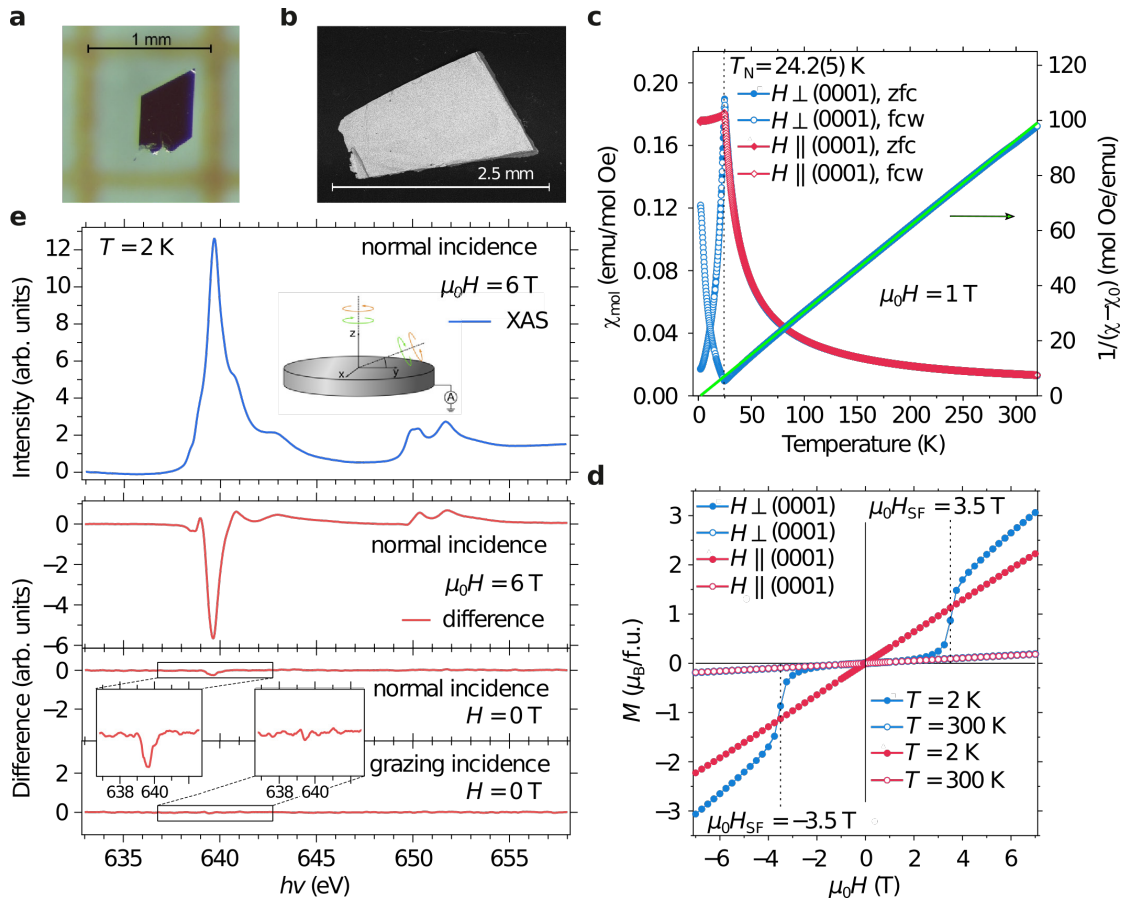


Figure 3

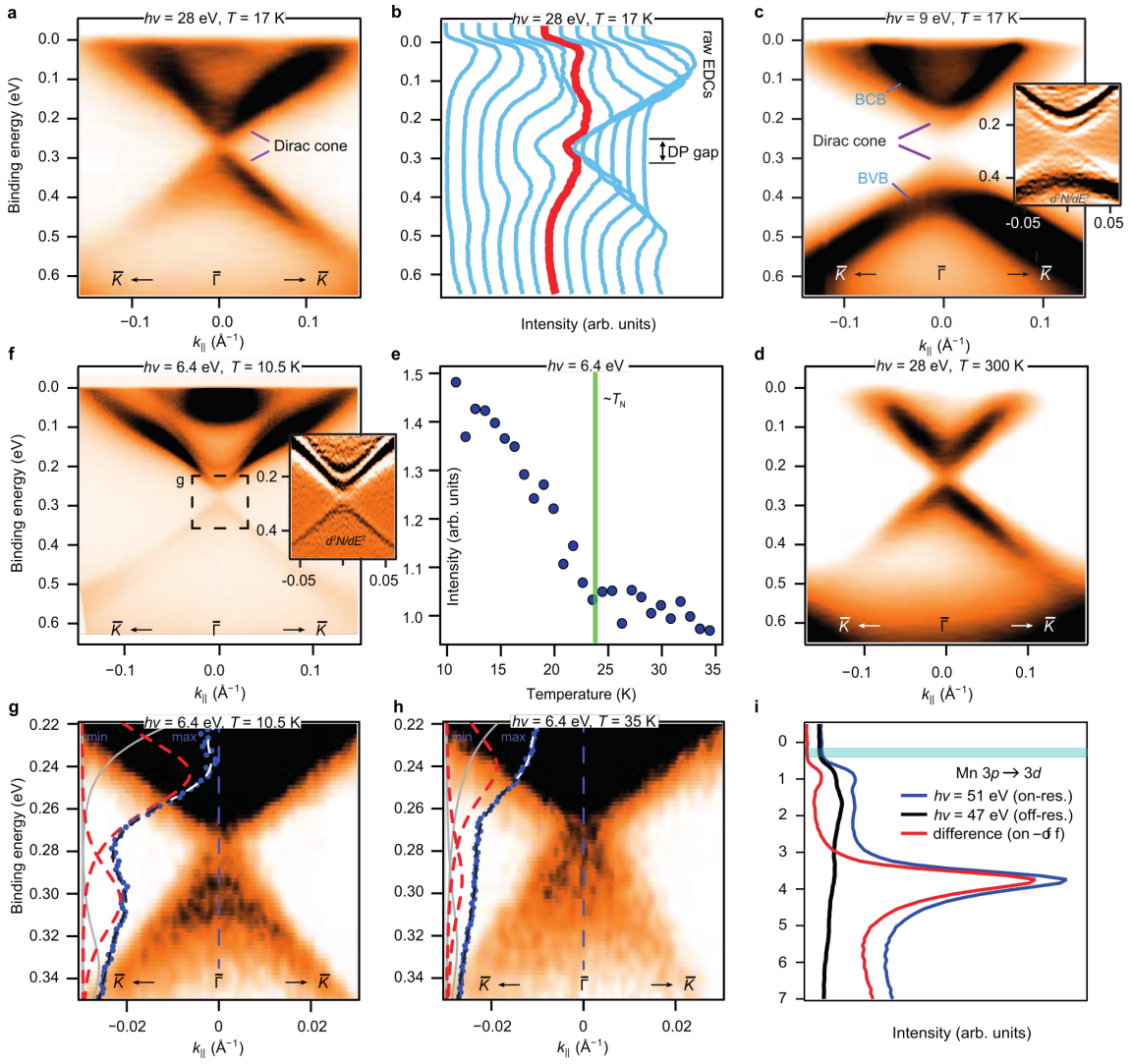
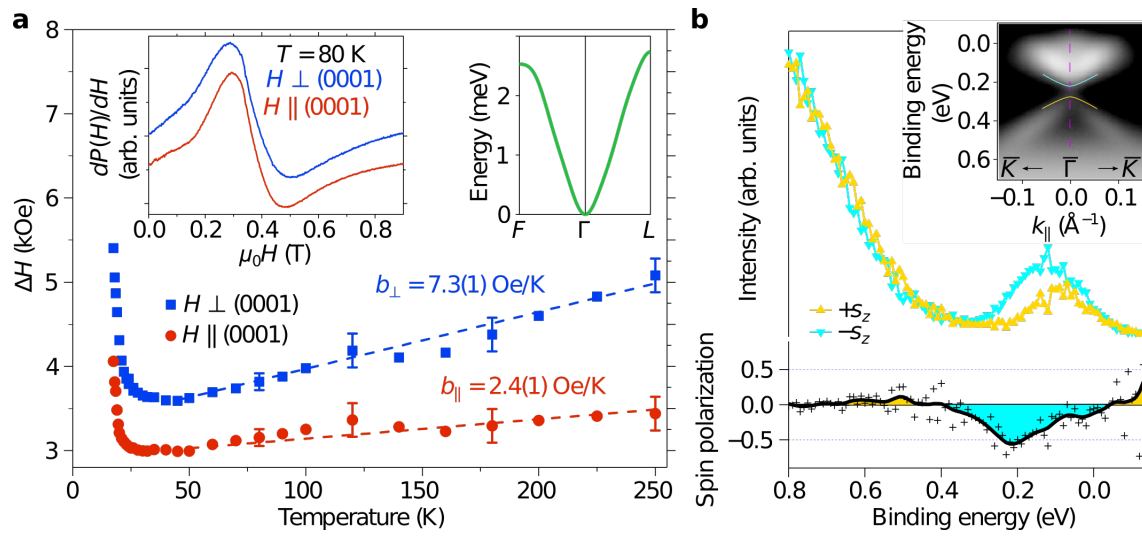
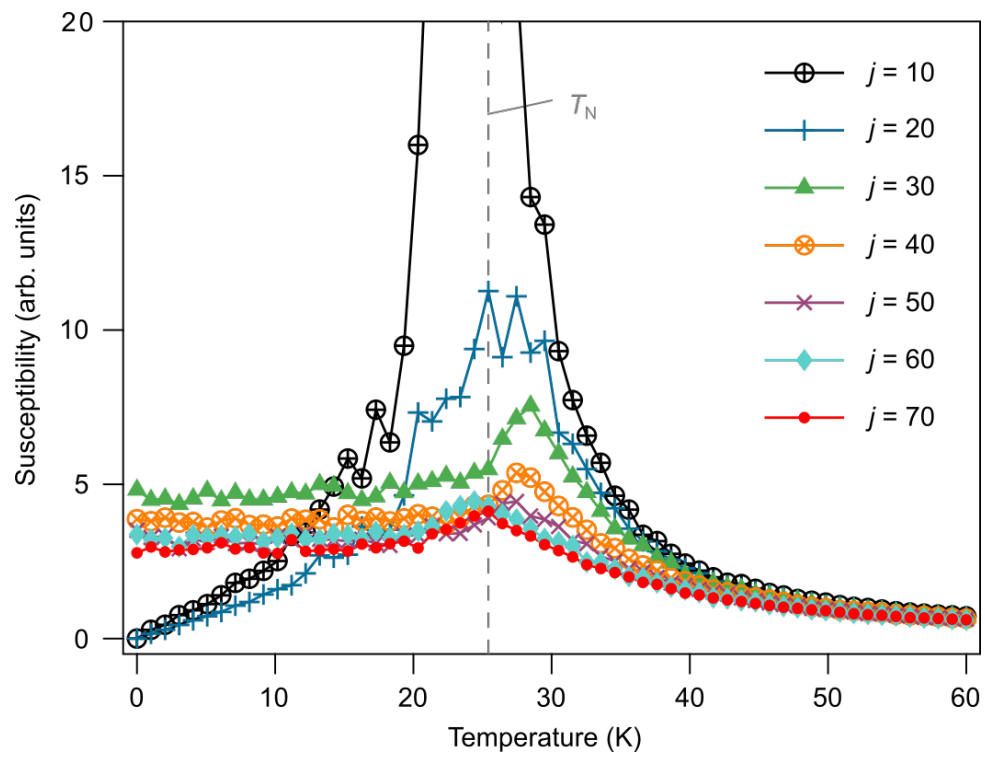


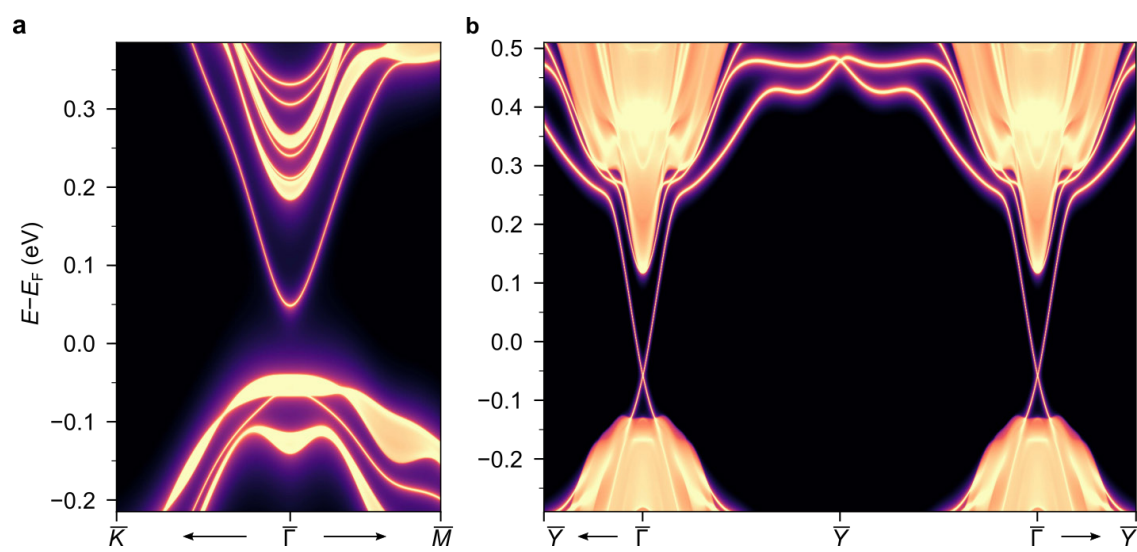
Figure 4



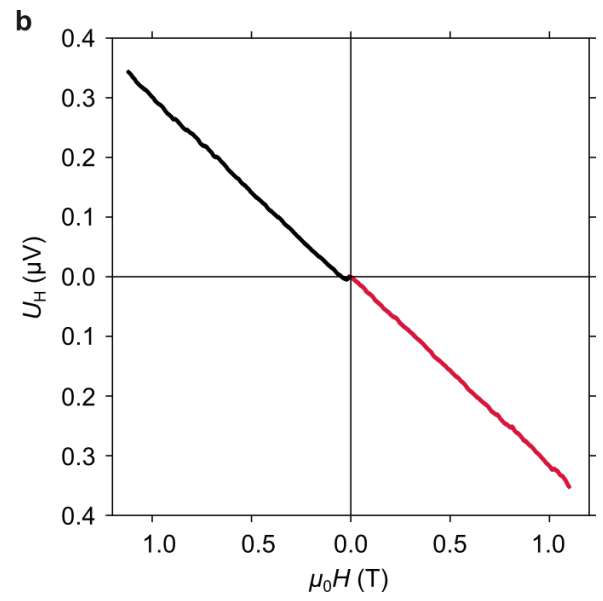
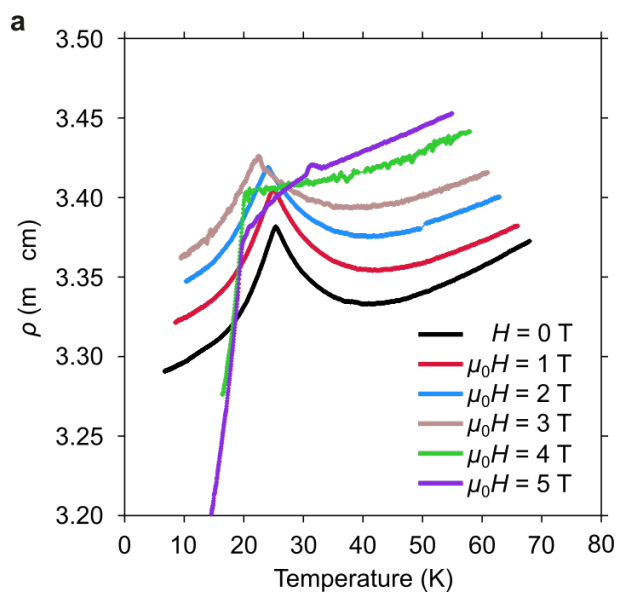
Extended Data Fig. 1



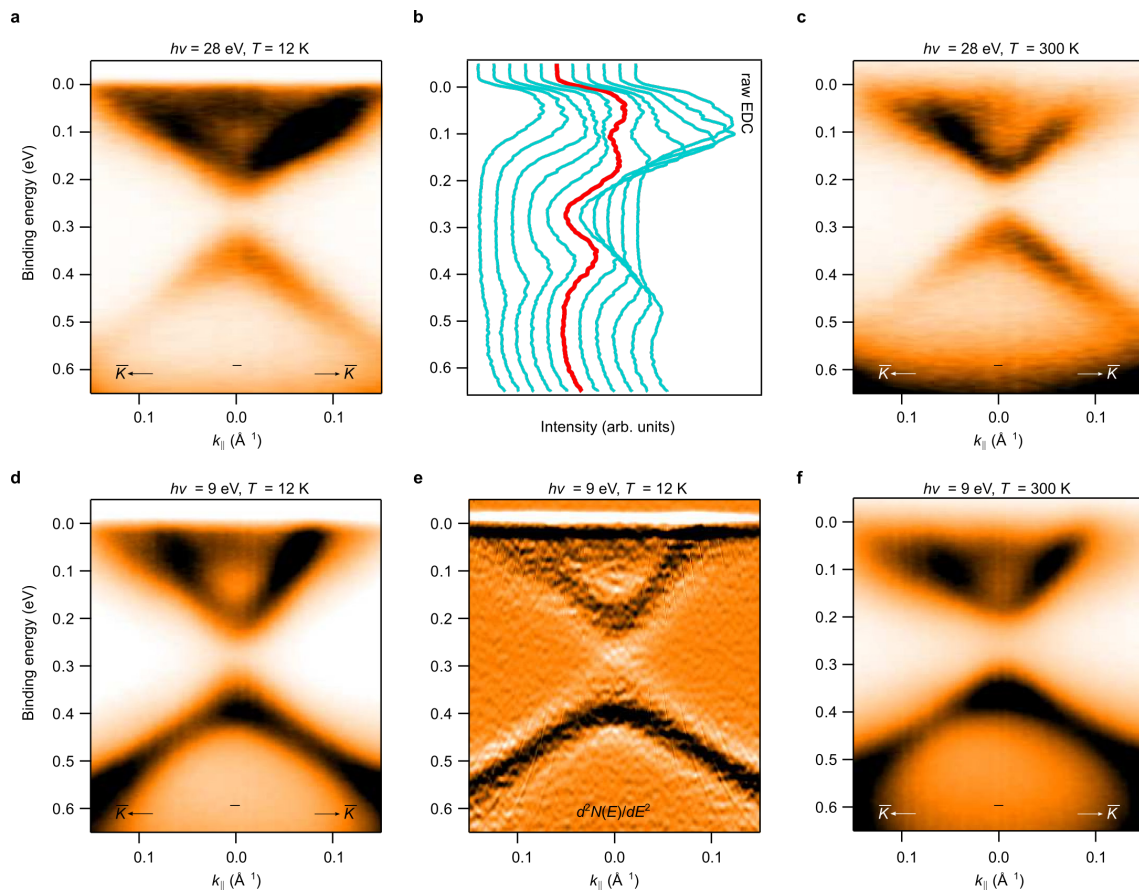
Extended Data Fig. 2



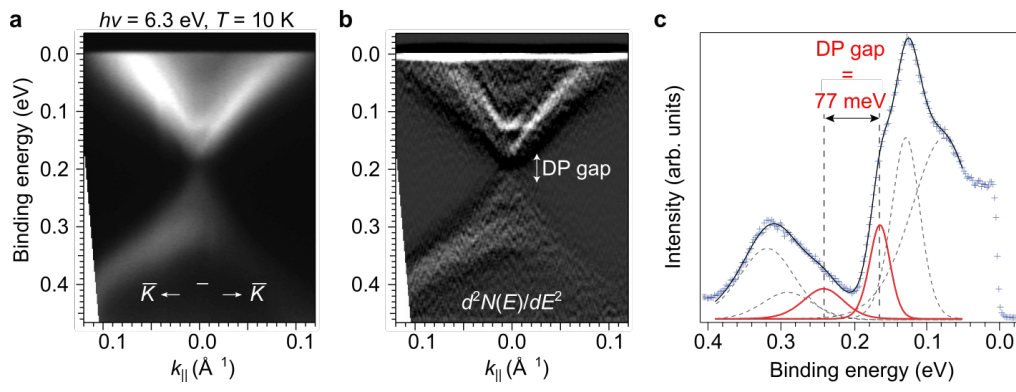
Extended Data Fig. 3



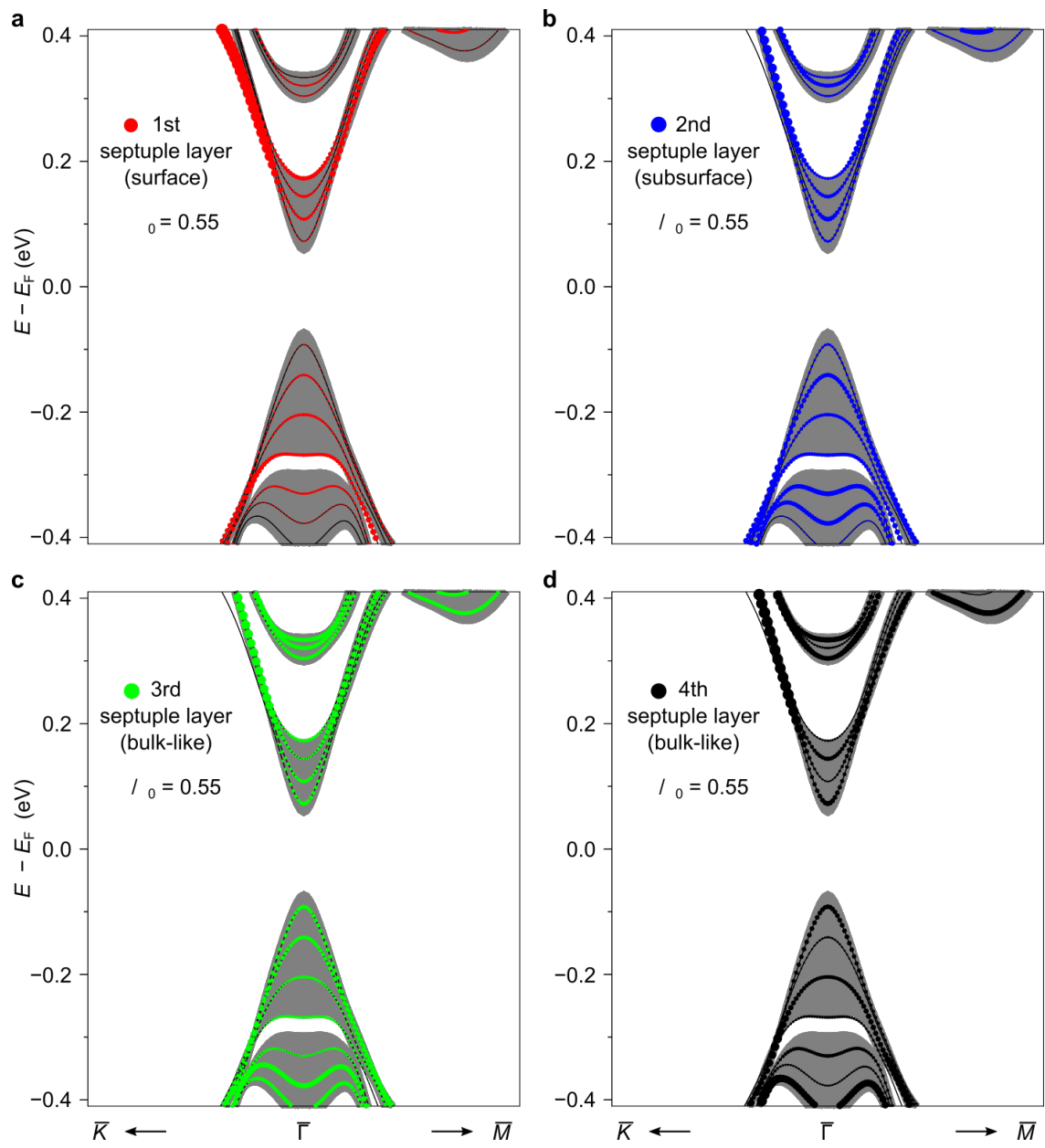
Extended Data Fig. 4



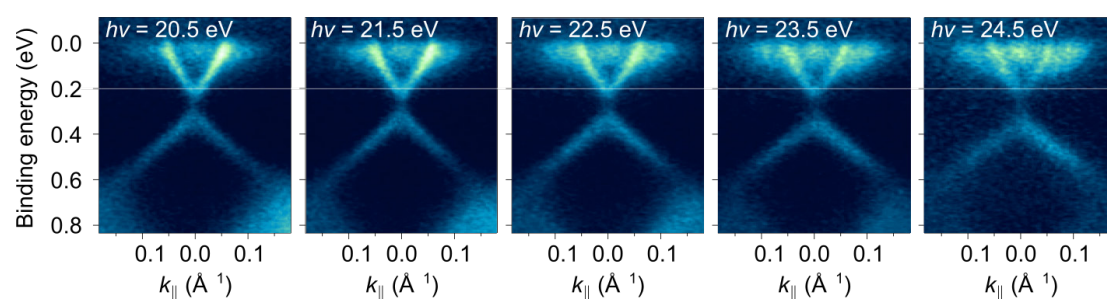
Extended Data Fig. 5



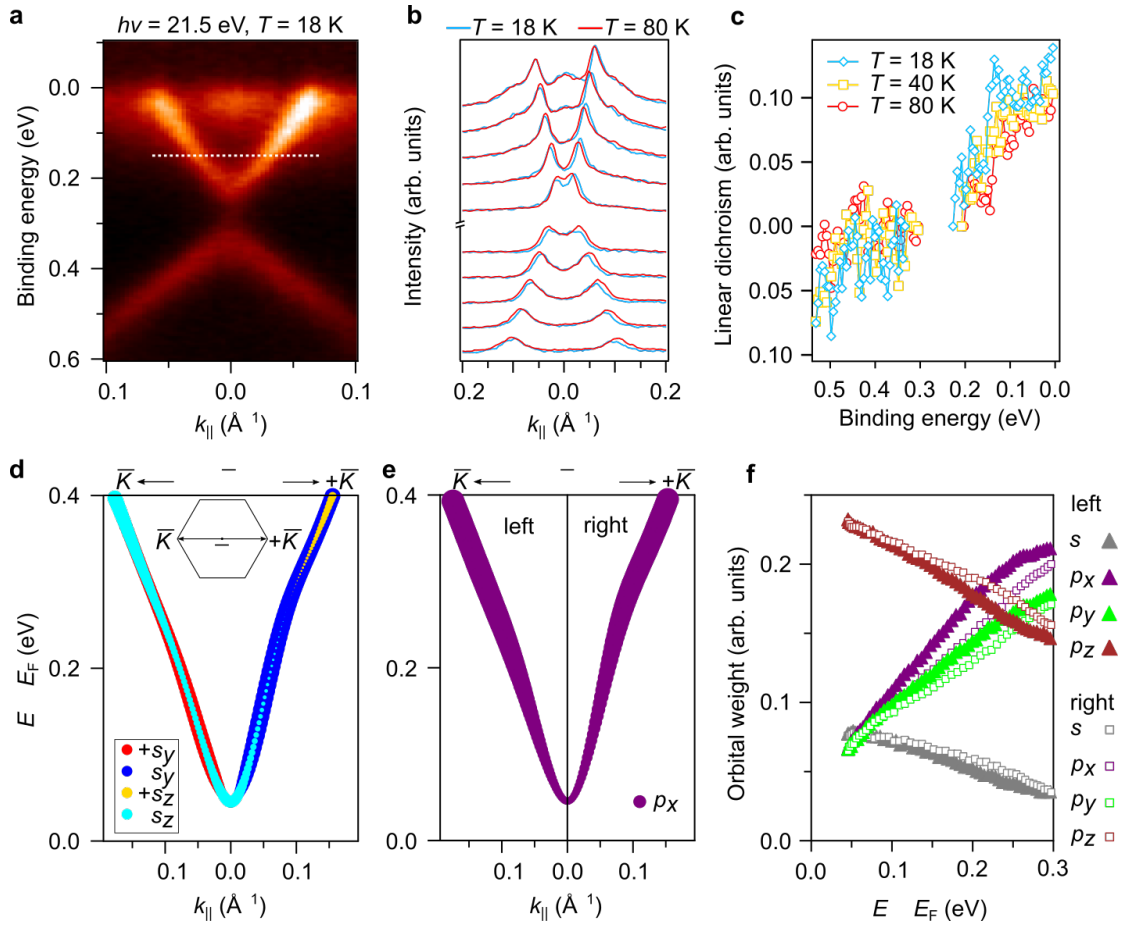
Extended Data Fig. 6



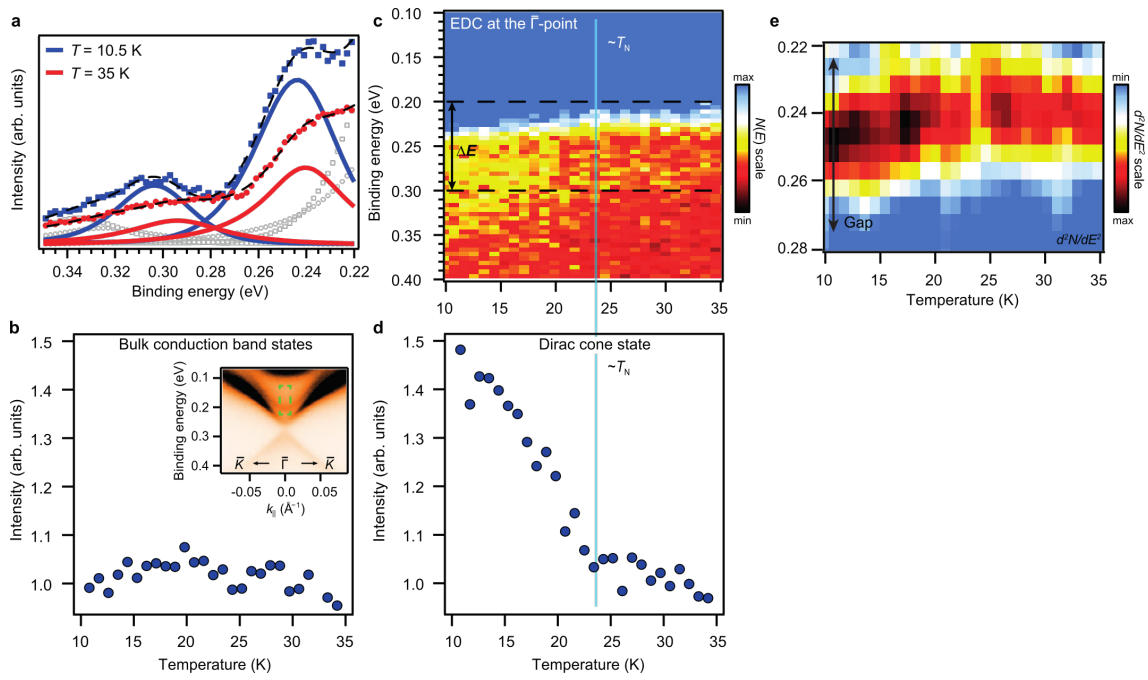
Extended Data Fig. 7



Extended Data Fig. 8



Extended Data Fig. 9



Extended Data Fig. 10

